Research Square

Preprints are preliminary reports that have not undergone peer review.
They should not be considered conclusive, used to inform clinical practice,
or referenced by the media as validated information.

CHD5 dysregulation causes epigenetic changes that dictate DNA double-strand break repair pathway choice and vulnerability to KMT5B/C inhibition

David Yu

dsyu@emory.edu

Emory University https://orcid.org/0000-0002-2781-5379

Sandip Rath

Winship Cancer Institute, Emory University, School of Medicine

Aleksandra Petrova

Winship Cancer Institute, Emory University, School of Medicine

Yitong Chan

Winship Cancer Institute, Emory University, School of Medicine

Ramona Haji-Seyed-Javadi

Emory University

Priya Kapoor-Vazirani

Emory University

Lydia Gutema

Winship Cancer Institute, Emory University, School of Medicine

Seohyun Kim

Winship Cancer Institute, Emory University, School of Medicine

Boya Gao

Duke University

Alicia Yin

Winship Cancer Institute, Emory University, School of Medicine

Anthony Sanchez

Winship Cancer Institute, Emory University, School of Medicine

Amanda Bastien

Emory University School of Medicine

Jimmy Patel

Winship Cancer Institute, Emory University, School of Medicine

Stevin Bienfait

Winship Cancer Institute, Emory University, School of Medicine

Steven Liang
Winship Cancer Institute, Emory University, School of Medicine
Roger Deal
Emory University
Xiaofeng Yang
Emory University
Zachary Buchwald
Emory University
Xingming Deng
Emory University https://orcid.org/0000-0003-0319-1511
Kyle Miller
Emory University https://orcid.org/0000-0002-4544-0013
Jennifer Spangle
Winship Cancer Institute of Emory University https://orcid.org/0000-0002-0181-3244
Sébastien Huet
University of Rennes https://orcid.org/0000-0002-3978-0003
Li Lan
Duke University https://orcid.org/0000-0003-0383-6172

Article

Keywords:

Posted Date: November 6th, 2026

DOI: https://doi.org/10.21203/rs.3.rs-8369060/v1

License: This work is licensed under a Creative Commons Attribution 4.0 International License.
Read Full License

Additional Declarations: There is **NO** Competing Interest.

CHD5 dysregulation causes epigenetic changes that dictate DNA double-strand break repair pathway choice and vulnerability to KMT5B/C inhibition

Sandip K. Rath[1], Aleksandra V. Petrova[1], Yitong Chen[1], Ramona Haji-Seyed-Javadi[1], Priya Kapoor-Vazirani[1], Lydia H. Gutema[1], Seohyun Kim[1], Boya Gao[2], Alicia Yin[1], Anthony Sanchez[1], Amanda J. Bastien[1], Jimmy S. Patel[1], Stevin Bienfait[1], Steven H. Liang[3], Roger B. Deal[4], Xiaofeng Yang[1], Zachary Buchwald[1], Xingming Deng[1], Kyle M. Miller[1], Jennifer M. Spangle[1], Sebastien Huet[5], Li Lan[2*], and David S. Yu[1*]

[1] Department of Radiation Oncology and Winship Cancer Institute, Emory University, School of Medicine, Atlanta, GA 30322, USA
[2] Duke University School of Medicine; 213 Research Drive, Durham, NC, 27710, USA
[3] Department of Radiology and Winship Cancer Institute, Emory University School of Medicine, Atlanta, GA 30322, USA
[4] Department of Biology, Emory University School of Medicine, Atlanta, GA 30322, USA
[5] Univ Rennes, CNRS, IGDR (Institut de génétique et développement de Rennes) – UMR 6290, BIOSIT (Biologie, Santé, Innovation Technologique) – UAR 3480, US 18, F35000 Rennes, France
*Correspondence: dsyu@emory.edu and li.lan@duke.edu

Running Title: CHD5 directs histone modifications in DSB repair

Abstract	145 words
Manuscript	(inclusive of materials and method section)
Figures	7 (Main), 7 (Supplemental)
References	115
Pages	50

Keywords: CHD5, chromatin, helicase, DNA repair, DNA damage response, end resection, homologous recombination, non-homologous end joining, HR, NHEJ, nucleosome, PARP, chromatin remodeling, epigenetics, SETD2, KMT5B, KMT5C

*Corresponding Authors:
David S. Yu, M.D., Ph.D.
Department of Radiation Oncology
Emory University School of Medicine
1365 Clifton Rd NE, C3008
Phone: 404-778-1758, Fax: 404-778-5520
e-mail: dsyu@emory.edu

Li Lan, PhD
Department of Molecular Genetics and Microbiology
Duke University School of Medicine
Durham, NC 27710 USA
Phone: 919-668-3003
email: li.lan@duke.edu

Summary (145)

The chromatin remodeler and helicase CHD5 is a tumor suppressor with broad relevance across several cancers. Here, we identify a role for CHD5 in the epigenetic control of DNA double-strand break (DSB) repair pathway choice. CHD5 is recruited to DSBs via PARP1/2-mediated chromatin relaxation where it acts to remodel the histone modification landscape to control repair pathway choice. We find that CHD5 promotes H3K36me3 deposition through the methyltransferase SETD2, enabling CtIP loading and homologous recombination (HR) repair of DSBs. CHD5 also suppresses KMT5B/C-dependent H4K20me2/3, which limits the recruitment of 53BP1 to DSBs and repair by non-homologous end joining (NHEJ). Therefore, our study illuminates how *CHD5* loss disrupts histone distribution at DSBs to drive genomic instability and create a vulnerability to KMT5B/C inhibition. These findings define an epigenetic mechanism governed by the CHD5 tumor suppressor whereby its loss rewires DSB repair and exposes a therapeutic opportunity.

Introduction

Chromodomain Helicase DNA Binding Protein 5 (CHD5) is a member of the SNF2 family of chromatin remodelers and is the only known CHD family member that functions as a bona fide tumor suppressor[1-3]. *CHD5* is located on chromosome 1p36, a genomic region frequently deleted in a broad range of human cancers, including neuroblastoma, hematological malignancies, glioma, breast cancer, renal cell carcinoma, melanoma, and colorectal carcinoma[4-13]. Its recurrent inactivation through multiple mechanisms, including loss of heterozygosity, somatic mutations, and epigenetic silencing, underscores its central role in tumor suppression[4, 7, 8, 14-24]. Significantly, in a murine model, germline deletion of *Chd5* is sufficient to drive spontaneous tumor development[8], supporting the functional relevance of CHD5 as a tumor suppressor *in vivo*. CHD5 has also been reported to function as prognostic factor in a number of cancers[11, 25-30]. Moreover, *CHD5* loss is implicated in 1p36 deletion syndrome[8, 12, 24, 31, 32], a developmental disorder characterized by congenital anomalies and neurodevelopmental deficits. These observations establish CHD5 as a disease-relevant chromatin remodeler; however, whether CHD5 plays a role in genome maintenance is unclear. Moreover, the impact of CHD5 dysregulation on DNA repair pathway choice and therapeutic vulnerability is not known.

A critical determinant of genome stability is the repair of DNA double strand breaks (DSBs)[33-35], lesions that, if left unresolved or inaccurately repaired, can result in indels and oncogenic chromosomal rearrangements[33]. Cells employ two major pathways to repair DSBs: non-homologous end joining (NHEJ), a rapid but error-prone process that ligates DNA ends without requiring sequence homology; and homologous recombination (HR), a high-fidelity pathway that uses a homologous sequence in the sister chromatid as a repair template, and is thus restricted to

the S and G2 phases of the cell cycle[33, 36]. The decision between these pathways is not stochastic but is tightly regulated by the chromatin landscape at the site of damage[36-41]. Chromatin acts as a dynamic signaling platform that is actively remodeled and chemically modified in response to DNA damage to facilitate DNA repair. Specific histone modifications, including acetylation, methylation, and ubiquitination marks, contribute to regulating the recruitment and activity of HR and NHEJ effectors[36-38, 40, 42-45]. The initiation and progression of HR are critically influenced by a permissive chromatin landscape. Histone acetylation marks such as H4K16ac and H4K8ac are associated with open chromatin and facilitate the recruitment of early HR sensors such as the MRN complex (MRE11-RAD50-NBS1)[43-45] while limiting Tumor Suppressor p53-Binding Protein 1 (53BP1) recruitment[46, 47]. HR is initiated by DNA end resection, a process involving 5′ to 3′ nucleolytic degradation to generate single-stranded DNA (ssDNA)[33-35, 48-51], a reaction that requires the CtBP-Interacting Protein (CtIP) endonuclease and is promoted by H3K36 trimethylation (H3K36me3) mediated by the SET Domain Containing 2, Histone Lysine Methyltransferase (SETD2)[48-50, 52-54]. The resected ssDNA is coated with Replication protein A (RPA) and subsequently replaced by the RAD51 recombinase to form a nucleoprotein filament that catalyzes strand invasion - steps that are also favored by accessible chromatin architecture[33]. In contrast, NHEJ is initiated when the Ku complex senses DSBs, subsequently facilitating the recruitment of 53BP1 through its binding to H4K20me1/2/3-marked histones[47, 55-62]. This, in turn, recruits Replication Timing Regulatory Factor 1 (RIF1), which stabilizes DNA ends and protects them from resection[63-67]. Thus, the fidelity of DSB repair hinges on the chromatin context and the proper deposition and interpretation of histone modifications at sites of damage. CHD5 is uniquely capable of partially unwrapping ~40–50 base pairs of DNA from nucleosome ends without repositioning the histone octamer[68], potentially enabling selective access to histone tails while

preserving pre-existing marks. This raises a central question: Does CHD5 control the histone modification balance that governs DSB repair pathway choice? If so, its frequent loss in cancer could disrupt this regulatory axis and create exploitable therapeutic vulnerabilities.

In this study, we elucidate a unique role for CHD5 in safeguarding genome stability by directing epigenetic cues necessary for accurate HR vs inaccurate NHEJ at DSBs for which *CHD5* dysregulation leads to genomic instability and vulnerability to KMT5B/C inhibition. We show that CHD5 is rapidly recruited to DNA damage sites following PARP-mediated chromatin relaxation, where it further promotes chromatin decompaction and facilitates SETD2-dependent deposition of H3K36me3, a histone mark critical for CtIP recruitment and DNA end resection and permissive to HR initiation. In contrast, *CHD5* deficiency promotes NHEJ by the accumulation of H4K20me1/2/3, thereby directing 53BP1 and in turn RIF1 recruitment. We further show that CHD5 coordinates the antagonistic recruitment of the histone methyltransferases SETD2 and KMT5B/C to DSB-proximal chromatin, thereby finetuning a repair-associated H3K36me3 and H4K20me2/3 histone code directed by CHD5 that mechanistically links chromatin remodeling, histone modification, and repair pathway choice. Our findings show that *CHD5* deficiency - present in a wide spectrum of cancers - disrupts this chromatin-based regulatory axis, resulting in impaired HR and a compensatory shift toward error-prone NHEJ leading to genomic instability and heightened sensitivity to epigenetic inhibition involving KMT5B/C, as well as inhibition of PARP and classical NHEJ factors.

Results

CHD5 ATPase-dependent helicase activity mediates resistance to DNA DSBs

To determine the role of CHD5 in responding to DNA damage, we investigated U2OS cells depleted for CHD5 for sensitivity to ultraviolet (UV) light, methyl methanesulfonate (MMS), bleomycin, etoposide, and ionizing radiation (IR). CHD5 depletion caused hypersensitivity to bleomycin, etoposide, and IR but not UV or MMS compared to a non-targeting (NT) control **(Fig. 1A-F)**, suggesting that CHD5 mediates resistance to agents that induce DSBs. CHD5 depletion also caused IR hypersensitivity in HEK293T, PANC1, and H460 cells **(Supplemental Fig. S1A-F)**, suggesting that the phenotype is not cell-type specific. Similar to CHD5 knockdown, IR hypersensitivity was observed in multiple U2OS *CHD5* knockout (KO) clones generated by CRISPR/Cas9 (**Supplemental Fig. S1G-H)** and could be alleviated by expression of CHD5-GFP wild-type (WT) but not D847A/D848A (DEAA), which abolishes its ATPase-dependent helicase activity[68] **(Fig. 1E-F and Supplemental Fig. S1E-H)**, suggesting that CHD5 helicase activity mediates resistance to DSBs, the phenotype is not due to an off-target effect, and that CHD5-GFP is functional for rescuing cell survival.

CHD5 localizes to and binds DSBs

To determine whether CHD5 localizes to DSBs, we performed proximity ligation assays (PLA) for endogenous CHD5 and γH2AX, a marker for DSBs. A significant increase in CHD5-γH2AX PLA foci was observed following treatment of U2OS cells with IR and etoposide, but not UV or MMS **(Fig. 1G-J and Supplemental Fig. S1I-L)**, suggesting that CHD5 specifically localizes to DSBs. Indeed, endogenous CHD5 localized to DNA damage sites induced by laser microirradiation, which were marked with the DNA damage signal γH2AX **(Fig. 1K)**, and mCherry-LacI-Fok1 endonuclease-induced DSBs in U2OS cells integrated with lac operator repeats[69] (**Fig. 1L)**, and moreover endogenous CHD5 also co-localized with I-SceI-induced DSBs

in U2OS-TRE-I-SceI-19 cells **(Supplemental Fig. S1N)**, validating CHD5 localization to DSBs. Additionally, we observed that CHD5 localizes to DSBs induced by laser-microirradiation in both cells in G1 and S/G2 cell cycle phases **(Supplemental Fig. S1O-P)**, suggesting that CHD5 localization to DSBs is not cell cycle specific. To determine whether CHD5 binds to DSBs, we performed chromatin immunoprecipitation (ChIP) with quantitative PCR (qPCR) and found an enrichment of CHD5 to Fok1-induced DSBs **(Fig. 1M)**. We also validated that CHD5 binds to both HR prone and NHEJ prone DSBs in U2OS DIvA cells[49, 70, 71] (150 AsiSI sequence specific-DSBs across the genome inducible via 4-hydroxytamoxifen) **(Fig. 1N)**. Collectively, these findings indicate that CHD5 localizes to and binds DSBs induced by multiple sources across multiple cell lines, independent of cell cycle stage.

PARP-mediated chromatin relaxation facilitates CHD5 localization to DSBs

Having identified the recruitment of CHD5 to DSBs, we next examined the underlying mechanism governing its mobilization to damage sites. To test this, we used a laser micro-irradiation assay in U2OS cells overexpressing CHD5-GFP. Treatment with the ATM inhibitor KU55933, ATR inhibitor VE821, or DNA-PKcs inhibitor NU7441 did not significantly affect CHD5 recruitment to DSBs **(Supplemental Fig. S2A-B)**. However, treatment with the poly ADP-ribose polymerase (PARP) inhibitor olaparib significantly decreased CHD5 recruitment **(Supplemental Fig. S2A-B)**, suggesting that PARP activity is essential for this process. A similar phenotype was observed upon siRNA-mediated depletion of PARP1 and PARP2 **(Supplemental Fig. S2C-D)**, suggesting that CHD5 recruitment is facilitated by both proteins and that the effect is not due to an off-target inhibitor effect. To determine if PARP enzymatic activity and/or trapping influences CHD5 recruitment to DSBs, we treated cells with olaparib and AG14361. Both inhibitors, olaparib (with

strong PARP trapping activity)[72, 73] and AG14361 (with weaker trapping activity)[74], were equally potent in impairing CHD5 recruitment **(Fig. 2A-B and Supplemental Fig. S2A-B)**, indicating that CHD5 localization depends on PARP enzymatic activity rather than trapping. Furthermore, ChIP-qPCR assays of CHD5 in U2OS-FokI cells validated that PARP1/2 facilitates CHD5 recruitment and binding to DSBs **(Fig. 2C-D)**. Next, co-immunoprecipitation of CHD5-FLAG in HEK293T cells revealed no evidence for CHD5 binding to or modification by poly(ADP-ribose) (PAR) chains **(Supplemental Fig. S2E)**, suggesting that CHD5 is neither PARylated nor directly interacts with PAR**.** Together, these data suggest that the presence and enzymatic activity of PARP1 and PARP2, but not direct PAR binding, are required for efficient CHD5 recruitment to DSBs. Indeed, to distinguish whether CHD5 recruitment to DSBs relies on PAR chain binding or PARP-mediated chromatin relaxation, we performed an independent assay in U2OS cells exposed to laser micro-irradiation. At 170 seconds post-irradiation, following PAR-dependent chromatin relaxation, we introduced PARPi to acutely inhibit PARP enzymatic activity. Under these conditions, proteins reliant on PAR chains, such as the WWE domain of RNF146[75-77], were quickly released from the irradiated area (**Fig. 2E-F)**. By 300 seconds post-irradiation, this protein was nearly completely absent from DNA lesions likely due to rapid PAR degradation by sustained PAR glycohydrolase activity. In contrast, CHD5, which is not PARylated, continued to accumulate **(Fig. 2G-H),** indicating that its recruitment does not require direct PAR binding. In a complementary approach, we compared CHD5 recruitment in U2OS cells overexpressing either ALC1 WT, a chromatin remodeler, whose ATPase activity drives chromatin relaxation at DNA damage sites or ALC1 E175Q, a catalytically inactive mutant[78, 79]. Our results showed that CHD5 accumulation at damage sites was impaired in cells overexpressing ALC1 E175Q but not WT **(Fig. 2I-J).** This result demonstrates that CHD5 recruitment depends on chromatin relaxation rather than PAR chain

binding. Collectively, these data imply that PARP activity-mediated chromatin relaxation facilitates the recruitment of CHD5 to DSBs.

CHD5 directs DSB repair pathway choice

PARP inhibitor sensitivity is associated with deficiency in HR[80, 81] . Indeed, CHD5 depletion in U2OS cells caused hypersensitivity to rucaparaib, veliparib, and talazoparib, which could be rescued by expression of CHD5-GFP WT but not DEAA **(Fig. 3A-C)**, suggesting that CHD5 may function in HR. Additionally, CHD5 depletion caused sensitivity to veliparib and next generation PARP inhibitors saruparib, a PARP1-selective inhibitor[82, 83], and UPF1035, a PARP2-selective inhibitor[84], in H460 cells **(Fig. 3D-F)**, suggesting that PARPi sensitivity phenotype is not specific to PARP1 or PARP2 activity or a particular cell type. To directly determine if CHD5 functions in HR, we examined CHD5 depletion in HEK293 and U2OS cells integrated with the direct-repeat (DR)-GFP reporter substrate in which expression of the I-SceI rare cutting endonuclease induces a DSB that when repaired by HR results in GFP expression[85-88]. CHD5 depletion caused an impairment in HR in both HEK293 and U2OS cells, which was alleviated by expression of CHD5-RFP WT but not DEAA **(Fig. 3G and H and Supplemental Fig. S3A and E)**, implying directly that CHD5 helicase activity promotes HR. To determine whether CHD5 functions in NHEJ, we examined CHD5 depletion in U2OS EJ5 total NHEJ (t-NHEJ), HEK293 EJ7 classical NHEJ (c-NHEJ), and U2OS EJ2 alternative NHEJ (alt-NHEJ) reporter cells[34, 35, 87, 88]. CHD5 depletion caused an increase in both t-NHEJ **(Supplemental Fig. S3B and F)** and c-NHEJ **(Fig. 3I and J)** but no significant difference in alt-NHEJ **(Supplemental Fig. S3C and G)**, suggesting that CHD5 plays a role in determining DSB repair by HR vs c-NHEJ but not alt-NHEJ. Importantly, no decrease in cells in S-phase was observed following CHD5 depletion in U2OS cells

(Supplemental Fig. S3D), suggesting that the observed phenotypes are not indirect effects of changes in cell cycle. Consistent with our findings, CHD5 depletion in U2OS cells impaired RAD51 localization to Fok1-induced DSBs **(Fig. 3K-L)** and IR-induced RAD51 foci **(Fig. 3M-N)**, and impaired etoposide and IR-induced RAD51 foci was observed in U2OS *CHD5* KO cells **(Supplemental Fig. S3H-I and L-M)**. In contrast, CHD5 depletion in U2OS cells caused an increase in RIF1 localization to Fok1-induced DSBs **(Fig. 3O-P)** and IR-induced RIF1 foci **(Fig. 3Q-R)**. An increase in etoposide and IR-induced RIF1 foci were also observed in U2OS CHD5 *KO* cells **(Supplemental Fig. S3J-K and Fig. S3N-O).** Collectively, these results suggest that CHD5 directs DSB repair pathway choice by promoting HR while suppressing c-NHEJ.

CHD5 helicase activity promotes DNA end resection

Given that DNA end resection is crucial for initiating HR and antagonistic to c-NHEJ[33, 89], we sought to examine the localization of RPA70, a protein that binds to ssDNA, following the induction of DSBs. CHD5 depletion in U2OS cells impaired RPA70 localization to Fok1-induced DSBs **(Fig. 4A-B)** and IR-induced RPA70 foci **(Fig. 4C-D)**. Consistent with this finding, CHD5 depletion also impaired RPA32 Ser4/8 phosphorylation[90] but not total RPA32 levels, which was alleviated by expression of CHD5-GFP WT but not catalytic dead DEAA **(Fig. 4E)**. To directly determine the role of CHD5 in DNA end resection, we labeled cells with BrdU, treated the cells with IR, and probed the cells for BrdU exposure under nondenaturing conditions to label ssDNA[91]. CHD5 depletion impaired BrdU exposure under these conditions, which was rescued by expression of CHD5-GFP WT but not DEAA **(Fig. 4F-G)**. To more quantitatively measure resection of ssDNA at DSBs, we performed qPCR of ssDNA at AsiSI-induced DSBs at RBMXL1 loci in DIvA cells[92] and measured ssDNA at 350, 1500, and 3500 base pairs (bp) upstream of the

DSB. A significant decrease in ssDNA was measured at each of these sites following CHD5 depletion, which was alleviated by CHD5-GFP expression **(Fig. 4H-I)**. As CtIP is involved in the early steps of DNA end resection[34, 35], we examined CtIP localization to DNA damage sites following CHD5 depletion. A significant impairment in CtIP-γH2AX PLA foci was observed following CHD5 depletion in U2OS cells **(Supplemental Fig. S4A-B)**. CHD5 depletion or knockout also impaired the localization of CtIP and/or GFP-CtIP to Fok1-induced DSB **(Fig. 4J-K)**, IR-induced foci **(Fig. 4L-M and Supplemental Fig. S4C-D)**, and DNA damage sites induced by laser micro-irradiation **(Supplemental Fig. S4E-F)**. As ATRIP localization to DNA damage sites is dependent on its interaction with RPA-ssDNA[93], we also examined its localization following CHD5 depletion and found an impairment in localization of GFP-ATRIP to DNA damage sites induced by laser micro-irradiation **(Supplemental Fig. S4G-H)**. These data demonstrate that CHD5 helicase activity is required for efficient DNA end resection, facilitating RPA and CtIP recruitment, and establishing a permissive substrate for HR.

CHD5 promotes chromatin relaxation at DSBs

Given its established role as a chromatin remodeler, we investigated whether CHD5 affects chromatin accessibility at DSBs using ATAC-seq in DIvA cells, with and without 4-OHT treatment. To precisely identify and map AsiSI-induced break sites, we next aligned our ATAC-seq results with DSB sites previously identified in an independent study by using breaks labeling *In Situ* and sequencing (BLISS) approach[94].Interestingly, our results showed a minimal change in chromatin accessibility at DSBs upon CHD5 knockdown in DIvA cells which were untreated for 4-OHT **(Fig. 5A)**. Conversely, CHD5 depleted cells challenged with 4-OHT showed a marked reduction in chromatin accessibility at DSBs **(Fig. 5B)**, suggesting that CHD5 promotes chromatin

relaxation at DSBs. Additionally, this change in accessibly was further validated upon CHD5 depletion at HR-prone DSBs in DIvA cells utilizing a PCR-based micrococcal nuclease assay **(Fig. 5C)**. Together, these results underscore CHD5's critical role in promoting chromatin relaxation at DSBs.

CHD5 ATPase-dependent helicase activity promotes H3K36me3

Histone H3K36me3 facilitates the recruitment of CtIP to DSBs via LEDGF, thereby promoting DNA end resection and HR[50, 52]. To determine whether CHD5-mediated chromatin remodeling activity promotes DNA end resection by facilitating specific histone modifications, we performed ChIP-qPCR at HR-prone DSBs in DIvA cells. CHD5 depletion at HR-prone DSBs led to a significant reduction in H3K36me3 but not H3K36me1 or H3K36me2, which was rescued by expression of CHD5-GFP WT but not DEAA **(Supplemental Fig. S5A-C)**. Importantly, CHD5 depletion in U2OS-265 cells, which are not biased towards HR or NHEJ, also resulted in decreased H3K36me3 at Fok1-induced DSBs **(Fig. 5D-E)**. This effect was rescued by CHD5-GFP WT but not DEAA. Moreover, global H3K36me3 levels remained unchanged following CHD5 depletion **(Supplemental Fig. S5G)**, suggesting that impaired H3K36me3 resulting from CHD5 deficiency is likely specific to DSB sites and not a result of overall turnover of H3K36me3 marks. These findings support CHD5-mediated chromatin relaxation at DSBs in creating a permissive environment for site-specific H3K36me3 deposition to promote DNA end resection and HR.

Impairment in CHD5 helicase activity increases NHEJ epigenetic marks at DSBs

Methylation states of histone H4 at lysine 20, particularly H4K20me2 and H4K20me3 facilitate c-NHEJ repair through the recruitment of 53BP1[55-63]. Given that CHD5 promotes HR, and its

depletion leads to an increase in c-NHEJ, we performed ChIP-qPCR upon CHD5 depletion at NHEJ-prone DSBs in DIvA cells. Consistent with the increased c-NHEJ phenotype observed, CHD5-depletion in DIvA cells showed an enrichment of H4K20me1, H4K20me2, and H4K20me3, which was rescued to a greater extent by expression of CHD5-GFP WT but not DEAA **(Supplemental Fig. S5D-F)**, suggesting that impairment in CHD5 helicase activity, at least in part, results in the increase of NHEJ epigenetic marks at DSBs and that there could also be a potential noncatalytic CHD5 role. Importantly, CHD5 depletion in unbiased U2OS-265 cells also showed enrichment of H4K20me1, H4K20me2, and H4K20me3 at Fok1-induced DSBs **(Fig. 5F-K)**. In contrast, we observed no significant change in global levels of H4K20me1, H4K20me2, and H4K20me3 following CHD5 depletion **(Supplemental Fig. S5G)**.

CHD5 directs recruitment of epigenetic writers to facilitate CtIP and 53BP1 binding at DSBs

SETD2 is the key methyltransferase known to catalyze H3K36me3[48, 49], and SETD2-dependent H3K36me3 is crucial for CtIP recruitment and promotion of DNA end resection and HR. Consistent with the impaired deposition of H3K36me3, we observed that CHD5 depletion in DIvA cells impairs the binding of SETD2 but not NSD1, NSD2, or NSD3, which catalyze H3K36me1 and H3K36me2, to HR-prone DSBs[95] **(Fig. 6A and Supplemental Fig. S6A-C)**. Moreover, a PLA assay showed that CHD5 depletion causes an impaired recruitment of SETD2 to DSBs in DIvA cells, which is rescued by expression of CHD5-GFP WT but not DEAA **(Fig. 6B-C)**, implying that CHD5 helicase activity promotes the recruitment of SETD2 to DSBs. Importantly, there was no significant decrease in expression of *SETD2* **(Supplemental Fig. S6D)**, indicating that the impaired recruitment of SETD2 to DSBs is not due to an indirect effect of decreased *SETD2* gene expression. Next, to determine whether CHD5 facilitates CtIP binding to DSBs, we

performed ChIP-qPCR following CHD5 depletion in DIvA and U2OS-265 cells. We observed a marked reduction in CtIP binding to HR-prone DSBs and Fok1-induced DSBs, which was rescued by expression of CHD5-GFP WT but not DEAA **(Fig. 6D)**. To investigate whether CHD5 and SETD2 act in a common pathway to promote HR, we performed an epistasis analysis using the DR-GFP reporter assay. Individual depletion of CHD5 or SETD2 resulted in a marked reduction in HR efficiency (**Fig. 6E-F**). Notably, concurrent depletion of both CHD5 and SETD2 did not further impair HR, suggesting that CHD5 and SETD2 function in a common pathway to facilitate HR. Collectively, these data indicate that CHD5-mediated chromatin relaxation facilitates SETD2 recruitment to DSBs to catalyze H3K36me3, which in turn promotes CtIP binding to DSBs to promote HR**.**

Given the role of KMT5 family methyltransferases in establishing H4K20me states[96], we used proximity ligation assays (PLA) to assess their recruitment to DSBs. CHD5 depletion in U2OS cells led to increased localization of KMT5A, KMT5B and KMT5C to DSBs **(Fig. 6G–J; Supplemental Fig. S6E–F)**. CHD5-GFP WT but not DEAA rescued the increased recruitment of KMT5C to DSBs **(Fig. 6I-J)**, while both CHD5-GFP WT and DEAA respectively partially alleviated and failed to alleviate the increased recruitment of KMT5B and KMT5A to DSBs **(Fig. 6G-H and Supplemental Fig. S6E-F)**, suggesting that CHD5 helicase activity limits KMT5C recruitment to DSBs while KMT5B recruitment to DSBs may be attributed to a non-catalytic role of CHD5 and the role of CHD5 in mediating KMT5A recruitment is unclear. ChIP-qPCR confirmed enhanced KMT5B binding to DSBs in CHD5-depleted cells **(Fig. 6K) (**similar assays for KMT5A and KMT5C were not feasible due to lack of ChIP-grade antibodies), and expression analysis suggested that these phenotypes are not an indirect result of transcriptional changes in

KMT5A-C **(Supplemental Fig. S6I–K)**. H4K20 methylation governs 53BP1 binding at DSBs to promote c-NHEJ[47, 55-61, 89]. In DIvA cells, CHD5 depletion led to increased enrichment of 53BP1 at NHEJ-prone DSBs, as measured by ChIP-qPCR, which was rescued by re-expression of CHD5-GFP WT but not DEAA **(Fig. 6L)**. Moreover, CHD5 depletion in U2OS-265 cells led to increased recruitment of both 53BP1 and its effector RIF1 **(Supplemental Fig. S6L–O)**. Collectively, these findings identify CHD5 as a regulator of KMT5C recruitment to DSBs via its ATPase activity, thereby limiting H4K20me2/3 deposition and downstream 53BP1-RIF1 loading. In contrast, KMT5A and KMT5B recruitment may be CHD5 helicase activity-independent, pointing to distinct regulatory mechanisms among KMT5 family members and a non-catalytic structural role of CHD5.

CHD5 deficiency leads to genomic instability

Given that CHD5 deficiency impairs HR but increases error-prone c-NHEJ, we next determined the extent to which CHD5 deficiency leads to spontaneous accumulation of 53BP1 nuclear bodies[97], a marker for genomic instability. An increase in 53BP1 nuclear bodies was observed following *CHD5* KO in U2OS cells or knockdown in U2OS or H460 cells compared with *CHD5* WT cells, which could be rescued at least in *CHD5* KO U2OS cells by expression of CHD5-GFP WT but not DEAA **(Fig. 7A-C and Supplemental Fig. S7A-D)**, suggesting that CHD5 helicase activity is critical for maintaining genome stability. CHD5 depletion in U2OS cells led to an increase in spontaneous accumulation of micronuclei[98] **(Fig. 7D-F)** and more directly, increased chromosomal breaks[99, 100] were observed in U2OS *CHD5* KO compared with WT cells **(Fig. 7G-H)**, providing further support that *CHD5* deficiency leads to genomic instability. To determine the association of CHD5 levels with genomic instability in patients, we examined The Cancer Genome

Atlas (TCGA) Pan-Cancer database[100, 101] and found an association of low CHD5 expression with low homologous recombination deficiency (HRD) score, high mutation count, high tumor mutation burden, and high aneuploidy score **(Fig. 7I and Supplemental Fig. S7E-G)**, suggesting that CHD5 deficiency in human patient tumors leads to genomic instability. Together, these cellular and patient clinical data demonstrate that CHD5 loss compromises accurate DNA repair and drives genomic instability, highlighting its role as a key genome caretaker.

CHD5 deficiency causes vulnerability to KMT5B/C-NHEJ inhibition

CHD5 depletion redirects DSB repair toward a 53BP1-dependent NHEJ pathway, generating a selective reliance on end-protection mechanisms[89]. As 53BP1 recruitment to DSBs is governed by H4K20me2/3 marks deposited by the methyltransferases KMT5B/C that are facilitated by CHD5, we hypothesized that disrupting this chromatin-based licensing step would unveil a therapeutic vulnerability in *CHD5*-deficient cells exposed to IR. Indeed, IR-treated H460 and H1299 cells depleted for CHD5 showed increased sensitivity to A196, a KMT5B/C inhibitor[102] **(Fig. 7J-L)**. To further substantiate that the observed sensitivity in *CHD*5-deficient cells arises from a compensatory reliance on the c-NHEJ pathway, we targeted core effectors of the DNAPKcs–XRCC4 axis. Indeed, CHD5 depletion in H460 cells, which was associated with an increase in IR-induced 53BP1 and RIF1 foci **(Supplemental Fig. S7H-K),** showed increased sensitivity to NHEJ inhibition of DNA-PK (Nu7441)[103], LIG1 (L189), and LIG4 (L189 and SCR7)[104] **(Supplemental Fig. S7L-O)**. Collectively, these findings indicate that *CHD5* deficiency fosters a dependency on the KMT5B/C-H4K20me2/3-53BP1 axis for efficient NHEJ, which causes synthetic lethality to epigenetic inhibition involving KMT5B/C and classical NHEJ factors.

Discussion

Our findings define an unrecognized role for the CHD5 tumor suppressor in directing histone modifications that govern DSB repair pathway choice for which *CHD5* loss disrupts this histone code, driving genomic instability and vulnerability to KMT5B/C inhibition. These findings identify CHD5 as a critical factor governing DSB repair pathway choice via regulation of a repair histone code, provide insight into how *Chd5* loss results in an *in vivo* tumor permissive phenotype, and reveal an epigenetic mechanism by which tumor suppressor loss rewires DSB repair pathway choice, which unmasks vulnerability to epigenetic inhibition. In this regard, we found that CHD5 helicase activity mediates resistance of multiple cancer types to DSB-inducing agents, and that CHD5 localizes and binds to DSBs in a manner facilitated by PARP1/2-mediated chromatin relaxation. CHD5 helicase activity further mediates resistance of cancer cells to PARP1/2 inhibition and *CHD5* deficiency causes impaired HR but increased c-NHEJ, demonstrating a role for CHD5 in promoting DSB repair pathway choice. Moreover, *CHD5* deficiency impairs DNA end resection that facilitates HR. Significantly, we found that CHD5 promotes chromatin relaxation at DSBs to facilitate H3K36me3, which directs CtIP recruitment to promote DNA end resection and HR. In contrast, *CHD5* deficiency leads to the accumulation of H4K20me2/3 at DSBs, thereby facilitating the recruitment of 53BP1 and in turn RIF1 to promote c-NHEJ. We further defined the mechanism for CHD5-directed histone marks by showing that CHD5 coordinates the antagonistic recruitment of SETD2 and KMT5B/C to DSBs, thereby finetuning a repair-associated H3K36me3 and H4K20me2/3 histone code directed by CHD5 that mechanistically links chromatin remodeling, histone modification, and repair pathway choice. As such, *CHD5* deficiency, which is prevalent in many cancers and causes increased error-prone NHEJ, leads to the spontaneous accumulation of 53BP1 nuclear bodies, micronuclei, and

chromosomal breaks in cancer cells and impaired HRD score, high mutational burden, and high aneuploidy in cancer patients, suggesting that CHD5's role in tumor suppression may, at least in part, be due to a role in promoting genome stability. Importantly, *CHD5* deficiency by augmenting c-NHEJ via H4K20me2/3 engenders vulnerability to epigenetic inhibition involving KMT5B/C as well as classical NHEJ factors, providing a rationale-driven therapeutic strategy for targeting CHD5 dysregulated cancers. Our findings thus lead to a model in which under conditions of *CHD5* proficiency, PARP1/2-mediated chromatin relaxation facilitates CHD5 localization and binding to DSBs **(Fig. 7M)**. CHD5 in turn remodels chromatin to facilitate SETD2 recruitment to breaks where it catalyzes H3K36me3 that binds CtIP to promote DNA end resection and HR, thereby promoting genome stability. In *CHD5* deficient cancers, SETD2-mediated H3K36me3 is impaired, whilst KMT5B/C are recruited to catalyze H4K20me2/3 which binds 53BP1 leading to error-prone c-NHEJ and genomic stability thereby causing vulnerability to inhibition of KMT5B/C as well as classical NHEJ factors.

CHD5 is a well-characterized tumor suppressor in multiple cancer types[4, 7, 8, 14-24] , including in a murine model whereby *Chd5* deficiency in a dosage-dependent manner leads to the spontaneous development of squamous cell carcinomas, lymphomas, and hibernomas *in vivo*[8]. Our finding that CHD5 chromatin remodeling activity promotes genome stability may help explain how CHD5 dysregulation leads to this *in vivo* tumor suppressive phenotype although our model is not mutually exclusive with other possibilities such as via CHD5 PHD-mediated histone H3 binding[105]. Consistent with our findings, *CHD5* deficiency has been reported to lead to the accumulation of DNA damage[29, 106], and an *in silico* analysis suggested that *CHD5* non-coding head and neck cancer variants lead to defective DNA repair[107]. Furthermore, low CHD5 levels in a number of

cancer types have consistently been reported to be associated with worse outcomes, including in pancreatic cancer[29], neuroblastoma[108], glioma[9, 109], renal cell carcinoma[11], gastric cancer[28], and colorectal cancer[110]. Given that CHD5 dysregulation leads to genomic instability, reduced HRD scores, increased mutational burden, and chromosomal instability, it is possible that this could could help explain how *CHD5* dysregulation may contribute to a more aggressive phenotype thereby leading to worse outcomes.

There is increasing evidence that DSB repair is regulated in the context of the chromatin landscape. Our findings define a critical role for CHD5 in promoting chromatin relaxation at DSBs to positively regulate SETD2-mediated H3K36me3 and negatively regulate KMT5B/C-mediated H4K20me2/3 that govern DSB repair pathway choice. Thus, these results support a model in which CHD5 controls an epigenetic code that dictates HR vs c-NHEJ permissive states at DSBs. Significantly, we found no evidence for a global change in H3K36me3 and H4K20me1-3 levels in the absence of DSBs, suggesting specificity for CHD5 in controlling histone modifications at DSBs vs global changes in histone methylation marks. It is possible that CHD5's unique chromatin remodeling activity in unwrapping nucleosomal DNA without disrupting nucleosome positioning may facilitate its activity at DSBs. It has been reported that H3K36me3 are pre-existing at DSBs[37, 48, 49, 111] while there is conflicting data on the induction of H4K20me1/2/3 at DSBs[37, 47, 56, 60, 62, 112, 113]. Our data suggest that CHD5-mediated chromatin remodeling may help maintain specific histone methylation states permissive to HR vs NHEJ. While our data indicate that CHD5 controls repair pathway choice at least in part via SETD2-mediated H3K36me3 and KMT5B/C-mediated H4K20me2/3, our model does not exclude the possibility that other histone modifications regulated by CHD5 such as H3K27me3, H3K27ac, and H4ac[106, 114] or other well-defined

epigenetic changes important for regulating DSB repair may also have a role and thus should be investigated in future studies. Furthermore, we found that the impairment in SETD2-mediated H3K36me3 of *CHD5* deficiency is rescued by expression of CHD5 WT but not DEAA, suggesting that CHD5 chromatin remodeling activity promotes SETD2-mediated H3K36me3. In contrast, while we found that the increase in H4K20me1-3 of *CHD5* deficiency is rescued to a greater extent by CHD5 WT compared with DEAA and the increase in KMT5C recruitment of *CHD5* deficiency is rescued by CHD5 WT but not DEAA, suggesting that CHD5 chromatin remodeling activity, at least in part, limits KMT5C-mediated H4K20me2/3, CHD5 DEAA also alleviated H4K20me1-3 and KMT5B recruitment, suggesting that there may also be a non-catalytic structural role for CHD5 in limiting KMT5B recruitment and H4K20me1-3, potentially by physically blocking KMT5B recruitment.

Given that CHD5 is a wide-spread tumor suppressor that is dysregulated in many cancer types, our finding that *CHD5* deficiency upregulates KMT5B/C mediated H4K20me2/3 and therefore engenders heightened sensitivity to KMT5B/C inhibition establishes a paradigm whereby tumor loss rewires epigenetic control of DSB repair to expose a therapeutic opportunity. Moreover, we found that *CHD5* deficiency causes synthetic lethality to DNA-PK, LIG1, LIG4, and PARP inhibition, providing rationale for treating CHD5 dysregulated cancers with multiple DNA repair targeted therapies.

Methods

Cell Culture

HEK293T, H460, PANC1 and U20S cell lines were purchased from the American Type Culture Collection (ATCC). U20S-235 mCherry-LacI-Fok1 cell line was a kind gift from Dr. Roger Greenberg. U20S-DR-GFP, U2OS-EJ5. U2OS-EJ2, HEK293-DR-GFP, and HEK293-EJ7 cell line was a kind gift from Dr. Jeremy Stark. Additionally, AsiSI-ER-U2OS (DIvA-DSB inducible via AsiSI) cells was obtained from Dr. Gaëlle Legube. All cell lines were cultured in DMEM (Dulbecco's Modified Eagle Medium). The U20S-235 cell line was cultured with the addition of 2 µg/mL puromycin and 100 µg/mL hygromycin. The DIvA cells were cultured with 1 µg/mL puromycin. HEK293-DR-GFP, and HEK293-EJ7 cells were seeded on poly-lysine (sigma #p4832) coated cell culture plates and additionally cultured in high glucose DMEM supplemented with L-glutamine but devoid of sodium pyruvate.

CHD5 Knockout cell generation

CHD5 guide RNA (gRNA) targeting exon 15 at GTTCTCCCGAATCACCGAG cloned in all-in-one Cas9-GFP and gRNA expression were purchased from sigma (Sigma#HSPD0000077294). Briefly, U2OS cells were transfected with the indicated guide RNAs, and 48 h post transfection cells were sorted for GFP positive population. The GFP-positive cells were then seeded in 96 well plates at a dilution of one cell per well. Cells were then allowed 4 weeks to recover to from single clones and subsequently analyzed for colonies positive for CHD5 knockout using western blot.

Transfections

For transfections 2-3 million cells were seeded in 60 mm plates and siRNA or cDNA of interest were transfected using Lipofectamine RNAi-Max, Lipofectamine 2000 or 3000 (Invitrogen) and performed as per the man- facture’s instructions. For overexpression 5 to 10 microgram of the

indicated plasmids were used. 4 hours post transfection fresh media were added and the cells were left to incubate for next 48-72 hours. The siRNA used in the study are listed in **Table 1**.

Cell and protein lysate treatments

To induce DNA damage U2OS and HEK293T cells were treated with 10 gray dosage of IR using X-Ray 320 irradiator (Precision X-Ray Inc., N. Brandford, CT). For inducing damage with UV treatment, cells were treated 50 J/m2 of UV for 3 h using Spectrolinker XL-1500 UV crosslinker (Spectronics Corp., Westbury, NY). The following drugs and inhibitors were used in the experiments Methyl methanesulfonate (MMS; Sigma # 129925), (TEVA pharmaceuticals), bleomycin (Selleckchem#s1214), BrdU (BD Biosciences # 347580), Veliparib (Selleckchem#s7048), Talazoparib (Selleckchem#s1004), Rucaparib (Selleckchem#s4948), Saruparib (Synthesized by lab of Steven Liang), UPF1035 (Synthesized by lab of Steven Liang), KU55933 (Selleckchem#s1092), VE821 (Selleckchem#s8007), NU7441 (Selleckchem#s2638). Cells were treated with 10 Gy of IR for 4 h using X-Ray 320 irradiator (Precision X-Ray Inc., N. Brandford, CT) and 50 J/m2 of UV for 3 h using Spectrolinker XL-1500 UV crosslinker (Spectronics Corp., Westbury, NY). To induce FOK1- or AsiSI-dependent DSB 1 μM Shield-1 (Takara # 632189) for 4 h; 2 mM or 500 nM 4-Hydroxytamoxifen (4-OHT; Sima # H7904) for 4 h were used, respectively.

Plasmids

CHD5-GFP and CHD5-RFP tagged plasmids were generated by cloning CHD5 into the EcoRI and BamH1 restriction sites of pcDNA3.1-GFP (Addgene#70219), pcDNA3.1-GFP (Addgene#13032), and pcDNA-3XFLAG (obtained from Emory Integrated Genomics Core)

respectively. GFP-CtIP were obtained from Dr. Steven Jackson (Sartori et al., 2007; Schmidt et al., 2015). ATRIP-GFP plasmid was obtained from Dr. Akira Matsuura (Itakura et al., 2005). Helicase mutant CHD5-GFP and RFP tagged plasmids were generated by introducing mutations D847A and D848 site using Quick-change site-directed mutagenesis kit (Agilent). pCBASceI expressing I-SceI endonuclease was obtained from Addgene. PA-GFP-H2A, GFP-WWE, ALC1 WT and ALC1E 175Q were kind gift from Dr. Sebastien Huet. Cas-9a/9b plasmids were kind gift from Dr. Jeremy Stark. Plasmid transfections were performed using lipofectamine 3000 reagent as per the manufacture's instruction.

BrdU foci DNA end resection assay

The BrdU assay was conducted following previously established protocols[34, 91]. In brief, U2OS cells transfected with the siRNA of interest (non-silencing or CHD5-UTR or CtIP) were seeded on coverslips and treated with 30 μM BrdU for 36 hours and then exposed for an additional 4h in presence of IR. Cells were then washed twice with ice-cold PBS and exposed to pre-extraction buffer 1 (containing 10 mM HEPES at pH 7.0, 100 mM NaCl, 3 mM $MgCl_2$, 300 mM sucrose, and 0.5% Triton X-100) for 20 minutes on ice. Cells were subsequently incubated using extraction buffer 2 (containing 10 mM Tris–HCl at pH 7.5, 10 mM NaCl, 3 mM $MgCl_2$, 0.5% sodium deoxycholate, and 1% Tween-20) for 15 minutes on ice. Cells were then washed thrice with ice-cold PBS, followed by fixing with 4%PFA and permeabilization with 0.1% PBST. Cells were then incubated overnight at 4 °C with a primary antibody specific to BrdU (obtained from Millipore) and DAPI (Southern Biotech # 0100-20) staining was performed to label the cell nuclei.

Clonogenic assay

U2OS, HEK293T, PANC1, H460, and H1299 cells silenced for endogenous CHD5, and U2OS cells silenced for endogenous CHD5 rescued with CHD5-GFP wildtype and mutants were plated and treated with various dosage of IR or concentrations of rucaparib, olaparib and talazoparib. Briefly, 500 cells was seeded for each condition. After 10-12 days of proliferation, surviving colonies containing 50 cells or more than that were counted and analyzed from three independent experiments. Plating efficiency (PE) was determined by dividing the number of colonies obtained by the number of cells seeded under untreated conditions. Surviving fractions were normalized according to the PE conditions.

Chromatin Immunoprecipitation (ChIP) assay

The ChIP assay was conducted using the ChromaFlashTM One-Step ChIP Kit (P-2025, Epigentek, Farmingdale, NY, USA) following the manufacturer's instructions. Briefly, DIvA cells were fixed with 1% formaldehyde (Sigma-252549) for 15 minutes at room temperature to crosslink DNA-protein interactions. The excessive crosslinking reaction of formaldehyde was quenched by adding 0.125 M glycine for 5 minutes. Cells were then washed three times with ice-cold PBS for 5 minutes each and cell lysate was prepared using lysis buffer containing (10 μM MG-132, 10% glycerol, 150 mM NaCl, and 50 mM Tris at pH 7.5) 0.375% CHAPS for histone writers and 1X RIPA buffer for histone marks. The lysed cells were then subjected to sonication using a Branson microtip SFX250 sonicator to fragment the chromatin into an average size of 500–800 base pairs. For immunoprecipitation, specific antibodies as described above in the antibodies section were used to selectively pull down the protein of interest along with its associated DNA sequences. As a negative control, IgG was used in place of the specific antibodies. For histones, H3 and H4 served as a positive control. The immunoprecipitated chromatin was then subjected to DNA isolation, and

quantitative real-time PCR was performed using PowerTrack™ SYBR Green Master Mix A46012 on a PCR 7500 Fast Real-Time PCR system (ThermoFisher). The assay utilized primers specific for various DNA regions, including HR1, HR2 and c-NHEJ prone repair sites in DIvA cells. The primers sequence utilized in this assay are listed in **Table 2**.

ChIP qPCR-based DNA end resection assay in DIvA cells.

Briefly, genomic DNA was isolated from DIvA cells treated with or without 4OHT. Approximately, 140 ng of genomic DNA was then digested with 20 units of restriction enzymes BsrG1 (NEB # R3575) or subjected to mock digestion using 1× NEB restriction enzyme buffer-4 at 37°C overnight. Later ~3 µl of digested DNA were used as template in a 25 µl qPCR reaction with 12.5 µl of PowerTrack™ SYBR Green Master Mix A46012, × 0.5 µM of forward and reverse primer. The qPCR was performed PCR 7500 Fast Real-Time PCR system (ThermoFisher). The percentage of single-stranded DNA (ss-DNA%) generated by resection at specific sites was calculated by the equation ssDNA% = 1/(2^(△Ct-1) + 0.5) *100, wherein for each sample, a △Ct value was calculated by subtracting the Ct value of the mock-digested sample from the Ct value of the digested sample. The primer sequence utilized in this assay are listed in **Table 3**.

ATAC-seq Sample Preparation and Analysis

ATAC-seq was performed to profile genome-wide chromatin accessibility. Fresh or cryopreserved cells (50,000 cells per sample) with viability >90% were submitted to Genewiz (Azenta Life Sciences, USA) for sample processing and library preparation. Cells were first washed with ice-cold phosphate-buffered saline (PBS) and lysed using a cold lysis buffer (10 mM Tris-HCl pH 7.4, 10 mM NaCl, 3 mM $MgCl_2$, 0.1% IGEPAL CA-630) to release intact nuclei. Nuclei were

immediately subjected to the transposition reaction using Tn5 transposase from the Nextera DNA Library Prep Kit (Illumina). This reaction simultaneously fragmented DNA and inserted sequencing adapters at regions of open chromatin and was carried out at 37°C for 30 minutes with gentle agitation.

Transposed DNA was purified using a silica column-based method and subsequently PCR-amplified using indexed primers. The optimal number of PCR cycles was determined by a side qPCR reaction to prevent amplification bias. The resulting libraries were size-selected (~200–700 bp) using dual-SPRI bead purification (AMPure XP) and assessed for quality and concentration using an Agilent Bioanalyzer and Qubit fluorometer, respectively. Libraries passing quality thresholds were sequenced on an Illumina NovaSeq platform, generating paired-end 2×50 bp reads, with an average depth of ~50 million read pairs per sample.

Dragen was used to trim adapters align paired end reads to the hg38 reference genome and remove duplicates. Bam files were processed using samtools such that the final bam file only contains high-quality, primary, properly mapped reads. Biological replicates were merged using the MergeSamFiles function in Picard. Bam files were normalized by counts per million (CPM) to account for differences in sequencing depth and converted to bigwig files with bamCoverage from deepTools. ATAC-seeq signal from the bigwig file was visualized using deepTools at annotated break sites in DIvA cells, as determined by Breaks Labeling *In Situ* and Sequencing (BLISS) at AsiSI motifs from a publicly available GEO dataset GSE97589[94]

FACS

Briefly, 50000 cells per ml U2OS cells were seeded in a 6-well plate treated with indicated siRNA for 48h. Post-transfection cells were washed twice with ice-cold PBS and fixed with 70% ethanol. Fixed cells were then treated with 50 µl of a 100 µg/ml stock of RNase inhibitor and 200 µl PI (from 50 µg/ml stock solution). Cells were then subjected to FACS to measure forward scatter (FS) and side scatter (SS) to identify single cells. The acquired population is then gated for cell cycle analysis using the Flow-Jo software.

Western Blotting

Harvested cells of interest were washed twice in PBS buffer and then resuspended in RIPA with 2% SDS with protease inhibitors except for probing histones and p-RPA. Cells were lysed for 1h on ice, and lysate was subjected to sonication for 10 sec on/off for 15 minutes. The sonicated lysates were then spun down at 15000g for 10 minutes and supernatant was collected. For probing CHD5, lysates were additionally treated with nuclease (Santa-cruz-cas 9025-65-4) (1µl from Stock for every 100µl lysate) as per manufacturer's recommendation. Protein concentration was determined using Bradford's reagent according to manufacturer's instructions. 50-100 µg of protein lysates were loaded onto SDS-PAGE gel and transferred to PVDF membrane to probe antibodies of interest.

Immunoprecipitation

Briefly, cells were harvested and washed twice with PBS. Cells were then lysed for 1 h on ice with 0.75% CHAPS buffer (10% (vol/vol) glycerol, 150 mM NaCl, 50 mM Tris pH 7.5, 0.75% CHAPS) with the cocktail protease inhibitors added fresh. The cells were then spun down at 15000g for 10

minutes at 4 °C and the resulting pellet were discarded. An equal volume of lysis buffer without CHAPS (10% (vol/vol) glycerol, 150 mM NaCl, 50 mM Tris pH 7.5) was added to the supernatant to dilute the total CHAPS concentration to 0.375%. The cell lysate was then precleared for 3 h with 30 µl of either protein G or A agarose beads. 10% of input was collected from the precleared lysate and rest of the supernatant was then IP'd overnight on a rotator at 4°C with antibodies pre-conjugated protein G or A agarose beads. Next day, the beads were washed thrice with 0.375% CHAPS buffer and finally resuspended in 20 µl of 0.375% CHAPS buffer (without inhibitor) and 4X SDS. The samples were then boiled for 7 minutes at 100°C, subsequently followed by centrifuging down at 8000g for 10 minutes. The supernatant was then collected and run on SDS-PAGE gel.

DNA repair reporter assay

HEK293 or U2OS stably integrated DR-GFP, EJ-5, EJ-2 and EJ-7 cells[86, 88, 115] were transfected with the indicated siRNA. 24h post transfection, fresh medium was added, and cells were transfected with either 2.5 µg I-SceI for HEK293 or U2OS DR-GFP, EJ-2 and EJ5 cells, except for EJ-7 cells were transfected with cas9a and cas9b guide RNAs. All the reporter cells were transfected with 3-5µg of either the empty RFP plasmid or the indicated CHD5-RFP rescue plasmid. 72 h post transfection, cells were harvested, washed twice with ice cold PBS. Cell pellet was then resuspended in 500 µl PBS and subjected to flow cytometry (Aurora Cytek) to measure GFP and RFP positive cells. Acquired FACS data was analyzed using the FlowJo software.

Real time quantitative PCR

Total RNA was extracted from cells using TRIzol Reagent (Life technologies, Carlsbad, USA), Subsequent RNA purification procedure was performed by PureLink RNA Mini Kit (Ambion, Carlsbad, USA) according to the manufacturer's protocol. Each experiment was done in triplicate with four internal replicates per sample. qPCR was performed on a 7500 Fast Real-Time PCR system (ThermoFisher). Results were analyzed using a paired two-tailed t test using GraphPad Prism. The primer sequence utilized in this assay are listed in Table 4.

Immunofluorescence

U20S cells were grown on coverslips and treated with indicated CHD5 siRNA with 10 Gy IR for 4 h. Post transfection coverslips were washed thrice with PBS and fixed in prechilled methanol for 20 minutes at 4^{o}C. Cells were then blocked for 1h with 5% BSA at room temperature and incubated with the indicated primary antibody overnight at 4^{o}C in humidified condition. Next day cells were washed thrice for 10 minutes with 0.1 % PBST (PBS with Tween-20) and then incubated with secondary antibodies for 1 hour each at 37^{o}C. To visualize nuclei cells was stained with DAPI and mounted on cover slides. Immunofluorescence signals were visualized either by Leica SP8 inverted confocal microscope at 63X magnification or on a Zeiss Observer Z1 microscope equipped with Axiovision Rel 4.8 software.

Antibodies, siRNA and Primers: Sequence and details of siRNA, all antibodies, qPCR, ChIP primers, and antibodies used in this study are provided in a separate excel sheet labelled as Table 1-5

Proximity ligation (PLA) assay

679 Briefly, cells were seeded at a density of 10^4 cells per well on cover slips. The cells were fixed and
680 permeabilized as described above in immunofluorescent assay. Cells were incubated then with
681 blocking buffer provided in the mouse/rabbit red starter Duolink kit (Olink, Uppsala, Sweden) for
682 2 hours at 37°C in a humidified chamber. The primary antibodies were then conjugated with the
683 probes provided within the kit and incubated for 1 hour at room temperature at 37°C in a
684 humidified chamber. They were then washed 3 times in Buffer A (provided in the kit). The cells
685 were then combined with amplification buffer and enzymes as per the manufacturer's protocol and
686 incubated for 90 minutes at 37°C. Next, cells were washed with 1x Buffer B (supplied with the
687 kit) for 10 minutes; this was followed by a 1-minute wash with 0.01X Buffer B. To visualize nuclei
688 cells was stained with DAPI supplied with the kit and mounted on cover slides. The red foci
689 indicated the proximity between 2 cellular-bound antibodies.
690
691 **MTT assay**
692 Cell viability was assessed using the MTT [3-(4,5-dimethylthiazol-2-yl)-2,5-diphenyltetrazolium
693 bromide] assay as described before. Briefly, H460 and H1299 cells were seeded into 96-well plates
694 at a density of 5,000 cells per well and allowed to adhere overnight. Cells were transfected with
695 control or CHD5-targeting siRNAs and treated with 4 Gray radiation and A916 inibitor
696 (selleckchem-Catalog No.S7983, stock 10 mM) as indicated. At the designated time points
697 (typically 96 hours post-transfection), 10 µL of MTT solution (5 mg/mL in PBS) was added to
698 each well and incubated at 37°C for 4 hours. The resulting formazan crystals were solubilized by
699 the addition of 100 µL DMSO, and absorbance was measured at 570 nm using a microplate reader
700 (with reference wavelength at 630 nm). Relative cell viability was normalized to untreated or
701 siRNA control-treated cells.

Resazurin Assay

Cell viability was assessed using the resazurin reduction assay. H460 cells were seeded at 7,500 cells/well in 96-well plates, treated as indicated, and incubated for 96 hours. Cells were transfected with control or CHD5-targeting siRNAs and treated with 4 Gray radiation and NHEJ inibitors DNAPKCs-Nu7441 (Selleckchem-S2638), Lig IV ihnibitor-SCR7 ((Selleckchem-S7742), Lig -I,III and IV inhibitor-L189 (Santacruz-cas 64232-83-3) as indicated Resazurin solution (Biotium-10054); 10 μL of 0.01% w/v was added to each well and incubated at 37°C for 4 hours. Fluorescence was measured at 560 nm excitation and 590 nm emission. Viability was calculated relative to control-treated cells.

Laser Microscopy

For laser micro irradiation 30,000 U2OS cells were plated on 35-mm glass bottom dishes (MatTek Corporation) and transfected with indicted CHD5-GFP, GFP-CtIP or GFP-ATRIP plasmids for 48 h. For CHD5 depletion induced impairment of CtIP or ATRIP, cells were transfected with indicated siRNA 12 hours post plasmid overexpression. Laser micro irradiation was performed on a Zeiss Observer Z1 microscope equipped with the Andor Micropoint® Laser Illumination and Ablation System (Photonic Instruments). The laser output was set to 85 %, and the GFP stripes were recorded at indicated time points and then analyzed with Fiji software. For assays involving endogenous proteins, localization to laser site cells were fixed in ice cold methanol post micro irradiation and visualized using 63X magnification Zeiss Observer Z1 microscope equipped with Axiovision Rel 4.8 software.

Statistical analysis

Statistical details of each experiment are explained in the figure legends. Statistical comparisons include two-tailed Student's t-test and one -way or two-way ANOVA analysis. Statistical comparisons are computed using Prism Software (GraphPad Version 9.3.1 (350), December 7, 2021). Statistical significance was set at * indicates $p<0.05$, ** indicates $p<0.01$; and *** indicates $p<0.005$. Data represented in graph are shown as mean and SEM from three independent replicas, unless stated otherwise.

Acknowledgments

We thank Dr. Roger Greenberg for U20S-235 mCherry-LacI-Fok1 cells, Dr. Jeremy Stark for U20S and/or 293-DR-GFP, EJ2, EJ5, and EJ7 cells, Dr. Gaelle Legube for AsiSI-ER-U2OS cells, Dr. Steve Jackson for GFP-CtIP plasmid, and Dr. Akira Matsuura for ATRIP-GFP plasmids. We would like to thank all the people who were involved in active discussion throughout the project. D.S.Y. is supported by National Institutes of Health (NIH)/National Cancer Institute (NCI) [R01CA178999, R01CA254403, R01CA301614, and U54CA274513] and Department of Defense (DOD) Breast Cancer Research Program (BCRP) BC220744. L.L is supported by NIH grant R01 CA282939 (LL). S.K.R. is supported by DOD Lung Cancer Research Program (LCRP) LC240534. K.M.M. is supported by NCI (RO1 CA198279 and CA250905), J.S.P. is supported by NCI T32CA275777 and the recipient of 2025 Elkin Fellowship. S.H.L. gratefully acknowledges the support provided, in part, by the NIH grant (AG094161), Emory Radiology Chair Fund, and Emory School of Medicine Endowed Directorship and A.S. is supported by a postdoctoral fellowship (PF-22-092-01-DMC) from the American Cancer Society.

Author contributions

S.K.R, D.S.Y., and L.L. conceived and designed the study. S.K.R., A.V.P., Y.C., R.H., P.K., L.H.G., S.K, B.G., A.Y., A.S., A.J.B., and S.H. performed and analyzed the experiments. S.K.R., A.V.P., Y.C., R.H., P.K., L.H.G., S.K., B.G., A.Y., A.S., A.J.B, S.B., R.B.D., X.Y., Z.B., X.Y., K.M.M, J.M.S., S.H., LL., and D.S.Y. interpreted the findings. S.K.R., D.S.Y., and L.L. wrote the manuscript with input from all authors.

Declaration of interests

The authors declare no competing interests.

759 **Figure Legends**

760 **Figure 1. CHD5 ATPase-dependent helicase activity mediates resistance to DNA DSBs and**
761 **CHD5 localizes to and binds to DSBs. A-D.** Colony survival assays in U2OS cells transfected
762 with CHD5 siRNA and exposed to indicated doses of ultraviolet-B (UV-B), methyl
763 methanesulfonate (MMS), bleomycin, or etoposide. Data represent mean ± SEM from three
764 independent replicates; ***$p < 0.001$. **E.** Colony survival assay in U2OS cells transfected with
765 three independent CHD5 siRNAs and rescued with CHD5-GFP wild-type (WT) or ATPase-dead
766 mutant (DEAA; D847A, E848A), followed by treatment with indicated doses of ionizing radiation
767 (IR). Data represent mean ± SEM from three independent replicates; ***$p < 0.001$. **F.** Western
768 blot confirming CHD5 knockdown and expression of CHD5-GFP WT and DEAA in U2OS cells
769 from panel (E). **G-J.** Representative proximity ligation assay (PLA) images and quantification of
770 CHD5-γH2AX co-localization in U2OS cells treated with 10 Gy IR or 10 μM etoposide for 4 h.
771 Data represent mean ± SEM from three independent replicates. **K.** Representative
772 immunofluorescence (IF) images showing CHD5 recruitment to sites of laser microirradiation-
773 induced DNA damage in U2OS cells fixed 5 min post-irradiation. **L.** Representative images
774 showing CHD5 localization at FokI-induced DSBs in U2OS-265 cells treated with 1 μM Shield-1
775 and 1 μM 4-OHT for 4 h. **M.** ChIP-qPCR analysis of CHD5 enrichment at the p1 and p4 DSB sites
776 in U2OS-265 cells following induction of DSBs using 1 μM Shield-1 and 1 μM 4-OHT for 4 h.
777 Data represent mean ± SEM from three independent replicates. **N.** ChIP-qPCR analysis showing
778 enrichment of CHD5, CtIP, and 53BP1 at control (no DSB), HR-prone (HR1, HR2), and c-NHEJ-
779 prone repair sites in DIvA cells following induction of DSBs with 500 nM 4-OHT for 4 h. Data
780 represent mean ± SEM from three independent replicates.
781

Figure 2. PARP mediated chromatin relaxation facilitates CHD5 localization to DSBs. A-B. Representative confocal images and quantification of CHD5-GFP recruitment kinetics in U2OS cells treated with or without 30 μM PARP inhibitor (PARPi, AG14361) following laser micro-irradiation. **C.** ChIP-qPCR analysis showing CHD5 enrichment at p1, p3, and p4 DSB sites in U2OS-265 cells transfected with indicated siRNAs targeting PARP1 or PARP2. DSBs were induced by treatment with 1 μM Shield-1 and 1 μM 4-OHT for 4 h. **D.** Western blot analysis confirming knockdown efficiency of PARP1 and PARP2 in U2OS-265 cells used in panel (C). **E-F.** Representative confocal images and quantification of GFP-WWE recruitment to laser-induced DNA lesions in U2OS cells treated with or without PARPi (AG14361). **G-H.** Representative confocal images and quantification of CHD5-GFP recruitment to laser-induced DNA lesions in U2OS cells treated with or without PARPi (AG14361). **I-J.** Representative images and quantification of CHD5-GFP recruitment kinetics following laser micro-irradiation in U2OS cells overexpressing ALC1 WT or ATPase-dead mutant (E175Q). Data represent mean ± SEM from three independent replicates. *$p < 0.05$, **$p < 0.01$, ***$p < 0.001$.

Figure 3. CHD5 directs DSB repair pathway choice. A-C. Colony survival assays in U2OS cells transfected with CHD5 siRNA and rescued with CHD5-GFP WT or DEAA, treated with increasing doses of the PARPi rucaparib (A), veliparib (B), or talazoparib. (C). **D-F.** Colony survival assays in H460 cells transfected with CHD5 siRNA, treated with increasing doses of veliparib (D), sauraparib (E), UPF1035 (F). **G.** Homologous recombination (HR) repair efficiency in HEK293 cells stably integrated with the DR-GFP HR reporter, transfected with indicated siRNAs and I-SceI, and rescued with CHD5-RFP WT or DEAA. RFP-positive cells were analyzed by flow cytometry, and the percentage of GFP-positive cells within this population was quantified

to assess HR activity. **H.** Western blot confirming CHD5 knockdown and expression of CHD5-RFP WT and DEAA in HEK293 DR-GFP cells used in panel (G). **I.** Classical non-homologous end joining (c-NHEJ) repair efficiency in HEK293 cells integrated with the EJ7-GFP reporter, transfected with indicated siRNAs and Cas9/sgRNA targeting the reporter locus. **J.** Western blot confirming CHD5 knockdown in HEK293 EJ7-GFP cells used in panel (I). **K-L.** Representative IF images and quantification of RAD51 (green) foci at FokI-mCherry–induced DSBs in U2OS-265 cells. Each dot represents a single cell. **K-L.** Representative IF images and quantification of RAD51 (purple) localization at FokI-mCherry–induced DSBs in U2OS-265 cells. Each dot represents a single cell. **M-N.** Representative IF images and quantification of RAD51 (red) and γH2AX (purple) foci in U2OS cells transfected with CHD5 or NT siRNAs and treated with 4 Gy IR for 4 h. Quantification is based on at least 150 cells; each dot represents an individual cell. **O-P.** Representative IF images and quantification of RIF1 (purple) localization at FokI-mCherry–induced DSBs in U2OS-265 cells. Each dot represents quantification from a single cell. **Q-R.** Representative IF images and quantification of RIF1 (red) and γH2AX (purple) foci in U2OS cells transfected with CHD5 or NT siRNAs and treated with 4 Gy IR for 4 h. Each dot represents an individual cell. Data in panels (A–E, I, K, M, O) represent mean ± SEM from three independent replicates. *$p < 0.05$, **$p < 0.01$, ***$p < 0.001$.

Figure 4. CHD5 helicase activity promotes DNA end resection. A-B. Representative IF images and quantification of RPA70 (green) and FokI-mCherry (red) localization in U2OS-265 cells transfected with CHD5 or NT siRNA, treated with 1 μM Shield-1 and 1 μM 4-OHT for 4 h. Data represent mean ± SEM from 150 cells across three independent replicates. ***$p < 0.001$. **C-D.** Representative IF images and quantification of γH2AX (red) and RPA70 (green) foci in U2OS

828 cells transfected with CHD5 or NT siRNA and treated with 10 Gy IR for 4 h. Data represent mean
829 ± SEM from 150 cells across three independent replicates. ***p < 0.001. **E.** Western blot analysis
830 of U2OS cells transfected with CHD5 or NT siRNA and rescued with CHD5-GFP WT or DEAA,
831 treated with 10 Gy IR, and harvested 4 h post-treatment. Blots were probed with the indicated
832 antibodies. **F-G.** Representative images and quantification of BrdU incorporation in γH2AX-
833 positive U2OS cells transfected with CHD5, CtIP, or NT siRNAs and rescued with CHD5-GFP
834 WT or DEAA. Cells were incubated with 30 μM BrdU for 36 h, treated with 10 Gy IR for 4 h, and
835 fixed under denaturing conditions for IF. Data represent the percentage of γH2AX-positive cells
836 with BrdU foci (mean ± SEM from three independent replicates).; *p < 0.00332, **p < 0.0021,
837 ***p < 0.0002. **H.** Quantitative PCR analysis of single-stranded DNA (ssDNA) at 350 bp, 1500
838 bp, and 3500 bp upstream of the RBMXL1 DSB site in DIvA cells transfected with CHD5 or NT
839 siRNA and rescued with CHD5-GFP WT. DSBs were induced with 500 nM 4-OHT for 4 h. Data
840 represent mean ± SEM from three independent replicates. *p < 0.00332, **p < 0.0021, ***p <
841 0.0002. **I.** Western blot confirming CHD5 knockdown and CHD5-GFP WT expression in DIvA
842 cells used in panel (H). **J-K.** Representative IF images and quantification of CtIP (green) and FokI-
843 mCherry (red) localization in U2OS-265 cells transfected with CHD5 or NT siRNA and treated
844 with 1 μM Shield-1 and 1 μM 4-OHT for 4 h. Data represent mean ± SEM from 150 cells across
845 four independent replicates. ***p < 0.001. **L-M.** Representative IF images and quantification of
846 CtIP (green) and γH2AX (red) foci in U2OS cells transfected with CHD5 or NT siRNA and treated
847 with 10 Gy IR for 4 h. Data represent mean ± SEM from 150 cells across four independent
848 replicates. ***p < 0.001.
849

Figure 5. CHD5-mediated chromatin relaxation directs HR and NHEJ histone methylation marks at DSBs. A-B. Representative ATAC-seq analysis showing chromatin accessibility in U2OS DIvA cells transfected with control or CHD5 siRNA and treated with or without 4-OHT at AsiSI induced DSBs. Biological duplicates are performed. **C.** Chromatin relaxation measured at HR1 repair-prone sites in DIvA cells using a micrococcal nuclease (MNase)-based qPCR assay. Cells were transfected with CHD5 or NT siRNA and treated with 4-OHT for 4 h. **D-E.** ChIP-qPCR analysis showing enrichment of H3K36me3 at p1 (D) and p4 (E) DSB sites in U2OS-265 cells transfected with CHD5 or NT siRNA, rescued with CHD5-GFP WT or DEAA, and treated with 1 μM Shield-1 and 1 μM 4-OHT for 4 h. **F-K.** ChIP-qPCR analysis showing enrichment of H4K20me1 (F, I), H4K20me2 (G, K), and H4K20me3 (H, K) at p1 and p4 DSB sites in U2OS-265 cells transfected with CHD5 or NT siRNA, rescued with CHD5-GFP WT or DEAA, and treated with 1 μM Shield-1 and 1 μM 4-OHT for 4 h. Data in panels (C–K) represent mean ± SEM from three independent replicates. *$p < 0.05$, **$p < 0.01$, ***$p < 0.001$.

Figure 6. CHD5 directs recruitment of epigenetic writers to facilitate CtIP and 53BP1 binding at DSBs. A. ChIP-qPCR analysis showing enrichment of SETD2 at HR1-prone DSB repair sites in U2OS DIvA cells transfected with CHD5 or NT siRNA and rescued with CHD5-GFP WT or DEAA, treated with or without 500 nM 4-OHT for 4 h. **B-C.** Representative PLA images and quantification showing SETD2–γH2AX co-localization in U2OS DIvA cells treated with or without 500 nM 4-OHT for 4 h. Nuclei were stained with DAPI (blue). Quantification was based on 50 nuclei from three independent replicates. **D.** ChIP-qPCR analysis of CtIP enrichment at HR1-prone repair sites in U2OS DIvA cells transfected with CHD5 or NT siRNA and rescued with CHD5-GFP WT or DEAA, treated with or without 500 nM 4-OHT for 4 h. **E.** HR repair

efficiency in U2OS cells stably integrated with the DR-GFP reporter, transfected with siRNAs targeting CHD5, SETD2, or CtIP along with I-SceI endonuclease. GFP-positive cells were quantified by flow cytometry. **F.** Western blot confirming CHD5 and SETD2 knockdown in U2OS DR-GFP reporter cells used in panel **G and H.** PLA images and quantification showing KMT5B–γH2AX co-localization in U2OS DIvA cells treated with or without 500 nM 4-OHT for 4 h. **I and J.** PLA images and quantification showing KMT5C–γH2AX co-localization in U2OS DIvA cells treated with or without 500 nM 4-OHT for 4 h. **K.** ChIP-qPCR analysis showing enrichment of KMT5B at c-NHEJ prone DSB repair sites in U2OS DIvA cells transfected with CHD5 or NT siRNA and treated with or without 500 nM 4-OHT for 4 h. **L.** ChIP-qPCR analysis showing enrichment of 53BP1 at c-NHEJ–prone DSB repair sites in DIvA cells transfected with CHD5 or NT siRNA and rescued with CHD5-GFP WT or DEAA, treated with or without 500 nM 4-OHT for 4 h. Data in panels **A**-**L** represent mean ± SEM from three independent replicates. *$p < 0.05$, **$p < 0.01$, ***$p < 0.001$.

Figure 7. CHD5 dysregulation causes genomic stability and vulnerability to KMT5B/C inhibitor. A-B. Representative images and quantification of 53BP1 nuclear bodies (red) in *CHD5* knockout (KO#3) U2OS cells rescued with CHD5-GFP WT or DEAA. Each dot represents a single cell. Data represent mean ± SEM from three independent replicates. ***$p < 0.001$. **C.** Western blot analysis confirming CHD5-GFP WT and DEAA expression in U2OS *CHD5* KO cells used in panels A-B. **D-E.** Representative IF images and quantification of micronuclei formation in CHD5-depleted U2OS cells. Each dot represents a single cell. Data represent mean ± SEM from three independent replicates. ***$p < 0.001$. **F.** Western blot confirming CHD5 knockdown in U2OS cells used in panel (D). **G-H.** Representative confocal images and quantification of metaphase

spread aberrations in U2OS *CHD5* KO cells. Data represent mean ± SEM from three independent replicates. ***p < 0.001. **I.** Heatmap retrieved from the UCSC Xena database showing that low CHD5 expression (blue) correlates with increased homologous recombination deficiency (HRD) score (red) across cancer patient samples. **J-K.** Cell viability assay in H460 and H1299 cells transfected with CHD5 or NT siRNA and treated with increasing concentrations of A196 (KMT5B/C inhibitor), followed by exposure to 4 Gy IR. Cell viability was measured 72 h post-treatment using the MTT assay. **L**. Western blot analysis of H460 cells transfected with indicated CHD5 siRNAs and A196 inhibitor. **M.** Model showing CHD5 governed DSB repair. **Left:** In CHD5-proficient cells, PARP recruits CHD5, which remodels chromatin at DSBs and promotes SETD2-mediated H3K36me3 deposition, enabling CtIP loading and high-fidelity homologous recombination (HR)**. Right:** In CHD5-deficient cells, loss of CHD5 favors KMT5B/C-mediated H4K20me2/3 and 53BP1 recruitment, blocking end resection and driving error-prone c-NHEJ. **Bottom:** CHD5-deficient tumors rely on c-NHEJ and are hypersensitive to KMT5B/C**,** NHEJ**,** and PARP inhibitors, revealing a therapeutic vulnerability.

1. Kolla, V., Zhuang, T., Higashi, M., Naraparaju, K. & Brodeur, G.M. Role of CHD5 in human cancers: 10 years later. *Cancer Res* **74**, 652-658 (2014).
2. Schuster, E.F. & Stöger, R. CHD5 defines a new subfamily of chromodomain-SWI2/SNF2-like helicases. *Mammalian Genome* **13**, 117-119 (2002).
3. Thompson, P.M., Gotoh, T., Kok, M., White, P.S. & Brodeur, G.M. CHD5, a new member of the chromodomain gene family, is preferentially expressed in the nervous system. *Oncogene* **22**, 1002-1011 (2003).
4. Lang, J., Tobias, E.S. & Mackie, R. Preliminary evidence for involvement of the tumour suppressor gene CHD5 in a family with cutaneous melanoma. *Br J Dermatol* **164**, 1010-1016 (2011).
5. Ng, D., Yang, X.R., Tucker, M.A. & Goldstein, A.M. Mutation screening of CHD5 in melanoma-prone families linked to 1p36 revealed no deleterious coding or splice site changes. *BMC Res Notes* **1**, 86 (2008).
6. Li, L. *et al*. A novel tumor suppressor encoded by a 1p36.3 lncRNA functions as a phosphoinositide-binding protein repressing AKT phosphorylation/activation and promoting autophagy. *Cell Death Differ* **30**, 1166-1183 (2023).
7. Fatemi, M. *et al*. Epigenetic silencing of CHD5, a novel tumor-suppressor gene, occurs in early colorectal cancer stages. *Cancer* **120**, 172-180 (2014).
8. Bagchi, A. *et al*. CHD5 is a tumor suppressor at human 1p36. *Cell* **128**, 459-475 (2007).
9. Wang, L. *et al*. Downregulation of chromatin remodeling factor CHD5 is associated with a poor prognosis in human glioma. *J Clin Neurosci* **20**, 958-963 (2013).
10. Henrich, K.O., Schwab, M. & Westermann, F. 1p36 tumor suppression--a matter of dosage? *Cancer Res* **72**, 6079-6088 (2012).
11. Huang, S. *et al*. Chromodomain Helicase DNA-Binding Protein 5 Inhibits Renal Cell Carcinoma Tumorigenesis by Activation of the p53 and RB Pathways. *Biomed Res Int* **2020**, 5425612 (2020).
12. White, P.S. *et al*. Definition and characterization of a region of 1p36.3 consistently deleted in neuroblastoma. *Oncogene* **24**, 2684-2694 (2005).
13. Baykara, O., Tansarikaya, M., Bulut, P., Demirkaya, A. & Buyru, N. CHD5 is a potential tumor suppressor in non small cell lung cancer (NSCLC). *Gene* **618**, 65-68 (2017).
14. Ma, Z. *et al*. Decreased expression of the CHD5 gene and its clinicopathological significance in breast cancer: Correlation with aberrant DNA methylation. *Oncol Lett* **12**, 4021-4026 (2016).
15. Naraparaju, K. *et al*. Role of microRNAs in epigenetic silencing of the CHD5 tumor suppressor gene in neuroblastomas. *Oncotarget* **7**, 15977-15985 (2016).
16. Zhao, R., Wang, N., Huang, H., Ma, W. & Yan, Q. CHD5 a tumour suppressor is epigenetically silenced in hepatocellular carcinoma. *Liver Int* **34**, e151-160 (2014).
17. Zhao, R., Meng, F., Wang, N., Ma, W. & Yan, Q. Silencing of CHD5 gene by promoter methylation in leukemia. *PLoS One* **9**, e85172 (2014).
18. Koyama, H. *et al*. Mechanisms of CHD5 Inactivation in neuroblastomas. *Clin Cancer Res* **18**, 1588-1597 (2012).

19. Cai, C. *et al*. MicroRNA-211 expression promotes colorectal cancer cell growth in vitro and in vivo by targeting tumor suppressor CHD5. *PLoS One* **7**, e29750 (2012).
20. Zhao, R. *et al*. CHD5, a tumor suppressor that is epigenetically silenced in lung cancer. *Lung Cancer* **76**, 324-331 (2012).
21. Wang, J. *et al*. The involvement of CHD5 hypermethylation in laryngeal squamous cell carcinoma. *Oral Oncol* **47**, 601-608 (2011).
22. Wang, X., Lau, K.K., So, L.K. & Lam, Y.W. CHD5 is down-regulated through promoter hypermethylation in gastric cancer. *J Biomed Sci* **16**, 95 (2009).
23. Gorringe, K.L. *et al*. Mutation and methylation analysis of the chromodomain-helicase-DNA binding 5 gene in ovarian cancer. *Neoplasia* **10**, 1253-1258 (2008).
24. Fujita, T. *et al*. CHD5, a tumor suppressor gene deleted from 1p36.31 in neuroblastomas. *J Natl Cancer Inst* **100**, 940-949 (2008).
25. Xu, L. *et al*. Pan-Cancer Analysis Identifies CHD5 as a Potential Biomarker for Glioma. *Int J Mol Sci* **23** (2022).
26. Laut, A.K. *et al*. CHD5 inhibits metastasis of neuroblastoma. *Oncogene* **41**, 622-633 (2022).
27. Yang, Z. *et al*. Mutations of METTL3 predict response to neoadjuvant chemotherapy in muscle-invasive bladder cancer. *J Clin Transl Res* **7**, 386-413 (2021).
28. Hashimoto, T. *et al*. Clinical significance of chromatin remodeling factor CHD5 expression in gastric cancer. *Oncol Lett* **19**, 1066-1073 (2020).
29. Hall, W.A. *et al*. Low CHD5 expression activates the DNA damage response and predicts poor outcome in patients undergoing adjuvant therapy for resected pancreatic cancer. *Oncogene* **33**, 5450-5456 (2014).
30. Liu, L., Wang, L., Zhang, H. & Yan, X. *J Formos Med Assoc* (2025).
31. Shimada, S. *et al*. Microarray analysis of 50 patients reveals the critical chromosomal regions responsible for 1p36 deletion syndrome-related complications. *Brain Dev* **37**, 515-526 (2015).
32. Okawa, E.R. *et al*. Expression and sequence analysis of candidates for the 1p36.31 tumor suppressor gene deleted in neuroblastomas. *Oncogene* **27**, 803-810 (2008).
33. Scully, R., Panday, A., Elango, R. & Willis, N.A. DNA double-strand break repair-pathway choice in somatic mammalian cells. *Nat Rev Mol Cell Biol* **1**, 019-0152 (2019).
34. Kapoor-Vazirani, P. *et al*. SAMHD1 deacetylation by SIRT1 promotes DNA end resection by facilitating DNA binding at double-strand breaks. *Nat Commun* **13**, 6707 (2022).
35. Daddacha, W. *et al*. SAMHD1 Promotes DNA End Resection to Facilitate DNA Repair by Homologous Recombination. *Cell Rep* **20**, 1921-1935 (2017).
36. Hauer, M.H. & Gasser, S.M. Chromatin and nucleosome dynamics in DNA damage and repair. *Genes Dev* **31**, 2204-2221 (2017).
37. Clouaire, T. *et al*. Comprehensive Mapping of Histone Modifications at DNA Double-Strand Breaks Deciphers Repair Pathway Chromatin Signatures. *Mol Cell* **72**, 250-262.e256 (2018).
38. Arnould, C. *et al*. Chromatin compartmentalization regulates the response to DNA damage. *Nature* **623**, 183-192 (2023).

39. Downs, J.A. & Gasser, S.M. Chromatin remodeling and spatial concerns in DNA double-strand break repair. *Curr Opin Cell Biol* **90**, 102405 (2024).
40. Ferrand, J., Plessier, A. & Polo, S.E. Control of the chromatin response to DNA damage: Histone proteins pull the strings. *Semin Cell Dev Biol* **113**, 75-87 (2021).
41. He, L. *et al*. The interplay between chromatin remodeling and DNA double-strand break repair: Implications for cancer biology and therapeutics. *DNA Repair (Amst)* **146**, 103811 (2025).
42. Green, C.M. & Almouzni, G. When repair meets chromatin. First in series on chromatin dynamics. *EMBO Rep* **3**, 28-33 (2002).
43. Sharma, G.G. *et al*. MOF and histone H4 acetylation at lysine 16 are critical for DNA damage response and double-strand break repair. *Mol Cell Biol* **30**, 3582-3595 (2010).
44. Renaud, E., Barascu, A. & Rosselli, F. Impaired TIP60-mediated H4K16 acetylation accounts for the aberrant chromatin accumulation of 53BP1 and RAP80 in Fanconi anemia pathway-deficient cells. *Nucleic Acids Res* **44**, 648-656 (2016).
45. Kim, J.J. *et al*. PCAF-Mediated Histone Acetylation Promotes Replication Fork Degradation by MRE11 and EXO1 in BRCA-Deficient Cells. *Mol Cell* **80**, 327-344.e328 (2020).
46. Shanbhag, N.M. & Greenberg, R.A. The dynamics of DNA damage repair and transcription. *Methods Mol Biol* **1042**, 227-235 (2013).
47. Hsiao, K.Y. & Mizzen, C.A. Histone H4 deacetylation facilitates 53BP1 DNA damage signaling and double-strand break repair. *J Mol Cell Biol* **5**, 157-165 (2013).
48. Pfister, S.X. *et al*. SETD2-dependent histone H3K36 trimethylation is required for homologous recombination repair and genome stability. *Cell Rep* **7**, 2006-2018 (2014).
49. Aymard, F. *et al*. Transcriptionally active chromatin recruits homologous recombination at DNA double-strand breaks. *Nat Struct Mol Biol* **21**, 366-374 (2014).
50. Li, L. & Wang, Y. Cross-talk between the H3K36me3 and H4K16ac histone epigenetic marks in DNA double-strand break repair. *J Biol Chem* **292**, 11951-11959 (2017).
51. Ceccaldi, R. & Cejka, P. Mechanisms and regulation of DNA end resection in the maintenance of genome stability. *Nat Rev Mol Cell Biol* **26**, 586-599 (2025).
52. Daugaard, M. *et al*. LEDGF (p75) promotes DNA-end resection and homologous recombination. *Nat Struct Mol Biol* **19**, 803-810 (2012).
53. Edmunds, J.W., Mahadevan, L.C. & Clayton, A.L. Dynamic histone H3 methylation during gene induction: HYPB/Setd2 mediates all H3K36 trimethylation. *Embo j* **27**, 406-420 (2008).
54. Carvalho, S. *et al*. SETD2 is required for DNA double-strand break repair and activation of the p53-mediated checkpoint. *Elife* **3**, e02482 (2014).
55. Botuyan, M.V. *et al*. Structural basis for the methylation state-specific recognition of histone H4-K20 by 53BP1 and Crb2 in DNA repair. *Cell* **127**, 1361-1373 (2006).
56. Tuzon, C.T. *et al*. Concerted activities of distinct H4K20 methyltransferases at DNA double-strand breaks regulate 53BP1 nucleation and NHEJ-directed repair. *Cell Rep* **8**, 430-438 (2014).

57. Jacquet, K. *et al*. The TIP60 Complex Regulates Bivalent Chromatin Recognition by 53BP1 through Direct H4K20me Binding and H2AK15 Acetylation. *Mol Cell* **62**, 409-421 (2016).
58. Campillo-Marcos, I., Monte-Serrano, E., Navarro-Carrasco, E., García-González, R. & Lazo, P.A. Lysine Methyltransferase Inhibitors Impair H4K20me2 and 53BP1 Foci in Response to DNA Damage in Sarcomas, a Synthetic Lethality Strategy. *Front Cell Dev Biol* **9**, 715126 (2021).
59. Li, Z., Bao, J., Qi, Y. & Zhang, J.Z.H. Computational approaches to studying methylated H4K20 recognition by DNA repair factor 53BP1. *Phys Chem Chem Phys* **22**, 6136-6144 (2020).
60. Pei, H. *et al*. MMSET regulates histone H4K20 methylation and 53BP1 accumulation at DNA damage sites. *Nature* **470**, 124-128 (2011).
61. Pellegrino, S., Michelena, J., Teloni, F., Imhof, R. & Altmeyer, M. Replication-Coupled Dilution of H4K20me2 Guides 53BP1 to Pre-replicative Chromatin. *Cell Rep* **19**, 1819-1831 (2017).
62. Svobodová Kovaříková, A., Legartová, S., Krejčí, J. & Bártová, E. H3K9me3 and H4K20me3 represent the epigenetic landscape for 53BP1 binding to DNA lesions. *Aging (Albany NY)* **10**, 2585-2605 (2018).
63. Chapman, J.R. *et al*. RIF1 is essential for 53BP1-dependent nonhomologous end joining and suppression of DNA double-strand break resection. *Mol Cell* **49**, 858-871 (2013).
64. Di Virgilio, M. *et al*. Rif1 prevents resection of DNA breaks and promotes immunoglobulin class switching. *Science* **339**, 711-715 (2013).
65. Escribano-Díaz, C. *et al*. A cell cycle-dependent regulatory circuit composed of 53BP1-RIF1 and BRCA1-CtIP controls DNA repair pathway choice. *Mol Cell* **49**, 872-883 (2013).
66. Feng, L., Fong, K.W., Wang, J., Wang, W. & Chen, J. RIF1 counteracts BRCA1-mediated end resection during DNA repair. *J Biol Chem* **288**, 11135-11143 (2013).
67. Zimmermann, M., Lottersberger, F., Buonomo, S.B., Sfeir, A. & de Lange, T. 53BP1 regulates DSB repair using Rif1 to control 5' end resection. *Science* **339**, 700-704 (2013).
68. Quan, J. & Yusufzai, T. The tumor suppressor chromodomain helicase DNA-binding protein 5 (CHD5) remodels nucleosomes by unwrapping. *J Biol Chem* **289**, 20717-20726 (2014).
69. Shanbhag, N.M., Rafalska-Metcalf, I.U., Balane-Bolivar, C., Janicki, S.M. & Greenberg, R.A. ATM-dependent chromatin changes silence transcription in cis to DNA double-strand breaks. *Cell* **141**, 970-981 (2010).
70. Iacovoni, J.S. *et al*. High-resolution profiling of gammaH2AX around DNA double strand breaks in the mammalian genome. *Embo j* **29**, 1446-1457 (2010).
71. Massip, L., Caron, P., Iacovoni, J.S., Trouche, D. & Legube, G. Deciphering the chromatin landscape induced around DNA double strand breaks. *Cell Cycle* **9**, 2963-2972 (2010).

72. Gopal, A.A., Fernandez, B., Delano, J., Weissleder, R. & Dubach, J.M. PARP trapping is governed by the PARP inhibitor dissociation rate constant. *Cell Chem Biol* **31**, 1373-1382.e1310 (2024).
73. Lin, X. *et al*. PARP inhibitors trap PARP2 and alter the mode of recruitment of PARP2 at DNA damage sites. *Nucleic Acids Res* **50**, 3958-3973 (2022).
74. Rudolph, J., Jung, K. & Luger, K. Inhibitors of PARP: Number crunching and structure gazing. *Proc Natl Acad Sci U S A* **119**, e2121979119 (2022).
75. Smith, R. *et al*. Poly(ADP-ribose)-dependent chromatin unfolding facilitates the association of DNA-binding proteins with DNA at sites of damage. *Nucleic Acids Res* **47**, 11250-11267 (2019).
76. Smith, R., Sellou, H., Chapuis, C., Huet, S. & Timinszky, G. CHD3 and CHD4 recruitment and chromatin remodeling activity at DNA breaks is promoted by early poly(ADP-ribose)-dependent chromatin relaxation. *Nucleic Acids Res* **46**, 6087-6098 (2018).
77. Rother, M.B. *et al*. CHD7 and 53BP1 regulate distinct pathways for the re-ligation of DNA double-strand breaks. *Nature Communications* **11**, 5775 (2020).
78. Ahel, D. *et al*. Poly(ADP-ribose)-dependent regulation of DNA repair by the chromatin remodeling enzyme ALC1. *Science* **325**, 1240-1243 (2009).
79. Gottschalk, A.J. *et al*. Poly(ADP-ribosyl)ation directs recruitment and activation of an ATP-dependent chromatin remodeler. *Proc Natl Acad Sci U S A* **106**, 13770-13774 (2009).
80. Bryant, H.E. *et al*. Specific killing of BRCA2-deficient tumours with inhibitors of poly(ADP-ribose) polymerase. *Nature* **434**, 913-917 (2005).
81. Farmer, H. *et al*. Targeting the DNA repair defect in BRCA mutant cells as a therapeutic strategy. *Nature* **434**, 917-921 (2005).
82. Illuzzi, G. *et al*. Preclinical Characterization of AZD5305, A Next-Generation, Highly Selective PARP1 Inhibitor and Trapper. *Clin Cancer Res* **28**, 4724-4736 (2022).
83. Johannes, J.W. *et al*. Discovery of 5-{4-[(7-Ethyl-6-oxo-5,6-dihydro-1,5-naphthyridin-3-yl)methyl]piperazin-1-yl}-N-methylpyridine-2-carboxamide (AZD5305): A PARP1-DNA Trapper with High Selectivity for PARP1 over PARP2 and Other PARPs. *J Med Chem* **64**, 14498-14512 (2021).
84. Pellicciari, R. *et al*. On the way to selective PARP-2 inhibitors. Design, synthesis, and preliminary evaluation of a series of isoquinolinone derivatives. *ChemMedChem* **3**, 914-923 (2008).
85. Pierce, A.J., Johnson, R.D., Thompson, L.H. & Jasin, M. XRCC3 promotes homology-directed repair of DNA damage in mammalian cells. *Genes Dev* **13**, 2633-2638 (1999).
86. Gunn, A. & Stark, J.M. I-SceI-based assays to examine distinct repair outcomes of mammalian chromosomal double strand breaks. *Methods Mol Biol* **920**, 379-391 (2012).
87. Seluanov, A., Mittelman, D., Pereira-Smith, O.M., Wilson, J.H. & Gorbunova, V. DNA end joining becomes less efficient and more error-prone during cellular senescence. *Proc Natl Acad Sci U S A* **101**, 7624-7629 (2004).

88. Bhargava, R. *et al*. C-NHEJ without indels is robust and requires synergistic function of distinct XLF domains. *Nature Communications* **9**, 2484 (2018).
89. Kakarougkas, A. *et al*. Opposing roles for 53BP1 during homologous recombination. *Nucleic Acids Res* **41**, 9719-9731 (2013).
90. Maréchal, A. & Zou, L. RPA-coated single-stranded DNA as a platform for post-translational modifications in the DNA damage response. *Cell Res* **25**, 9-23 (2015).
91. Mukherjee, B., Tomimatsu, N. & Burma, S. Immunofluorescence-based methods to monitor DNA end resection. *Methods Mol Biol* **1292**, 67-75 (2015).
92. Domingo-Prim, J. *et al*. EXOSC10 is required for RPA assembly and controlled DNA end resection at DNA double-strand breaks. *Nat Commun* **10**, 2135 (2019).
93. Ball, H.L., Myers, J.S. & Cortez, D. ATRIP binding to replication protein A-single-stranded DNA promotes ATR-ATRIP localization but is dispensable for Chk1 phosphorylation. *Mol Biol Cell* **16**, 2372-2381 (2005).
94. Iannelli, F. *et al*. A damaged genome's transcriptional landscape through multilayered expression profiling around in situ-mapped DNA double-strand breaks. *Nature Communications* **8**, 15656 (2017).
95. Wagner, E.J. & Carpenter, P.B. Understanding the language of Lys36 methylation at histone H3. *Nat Rev Mol Cell Biol* **13**, 115-126 (2012).
96. Husmann, D. & Gozani, O. Histone lysine methyltransferases in biology and disease. *Nat Struct Mol Biol* **26**, 880-889 (2019).
97. Lukas, C. *et al*. 53BP1 nuclear bodies form around DNA lesions generated by mitotic transmission of chromosomes under replication stress. *Nat Cell Biol* **13**, 243-253 (2011).
98. Krupina, K., Goginashvili, A. & Cleveland, D.W. Causes and consequences of micronuclei. *Curr Opin Cell Biol* **70**, 91-99 (2021).
99. Paniagua, I. & Jacobs, J.J.L. Quantification of Chromosomal Aberrations in Mammalian Cells. *Bio Protoc* **13**, e4739 (2023).
100. Cerami, E. *et al*. The cBio cancer genomics portal: an open platform for exploring multidimensional cancer genomics data. *Cancer Discov* **2**, 401-404 (2012).
101. Goldman, M.J. *et al*. Visualizing and interpreting cancer genomics data via the Xena platform. *Nature Biotechnology* **38**, 675-678 (2020).
102. Bromberg, K.D. *et al*. The SUV4-20 inhibitor A-196 verifies a role for epigenetics in genomic integrity. *Nat Chem Biol* **13**, 317-324 (2017).
103. Leahy, J.J. *et al*. Identification of a highly potent and selective DNA-dependent protein kinase (DNA-PK) inhibitor (NU7441) by screening of chromenone libraries. *Bioorg Med Chem Lett* **14**, 6083-6087 (2004).
104. Chen, X. *et al*. Rational design of human DNA ligase inhibitors that target cellular DNA replication and repair. *Cancer Res* **68**, 3169-3177 (2008).
105. Paul, S. *et al*. Chd5 requires PHD-mediated histone 3 binding for tumor suppression. *Cell Rep* **3**, 92-102 (2013).
106. Li, W. *et al*. Chd5 orchestrates chromatin remodelling during sperm development. *Nat Commun* **5**, 3812 (2014).

107. Das, R., Kundu, S., Laskar, S., Choudhury, Y. & Ghosh, S.K. In silico assessment of DNA damage response gene variants associated with head and neck cancer. *J Biomol Struct Dyn* **41**, 2090-2107 (2023).
108. Laut, A.K. *et al*. CHD5 inhibits metastasis of neuroblastoma. *Oncogene* **41**, 622-633 (2022).
109. Haghshenas, Z., Nazari, E., Khalili-Tanha, G. & Razzaghi, Z. Identification of Prognostic and Diagnostic Biomarkers for Glioma Utilizing Immune System Gene Profiling. *Med J Islam Repub Iran* **39**, 49 (2025).
110. Zhou, Y. *et al*. Expression of CHD5 may serve as an independent biomarker of prognosis in colorectal cancer via immunohistochemical staining. *Int J Clin Exp Pathol* **11**, 2792-2798 (2018).
111. Fnu, S. *et al*. Methylation of histone H3 lysine 36 enhances DNA repair by nonhomologous end-joining. *Proc Natl Acad Sci U S A* **108**, 540-545 (2011).
112. Hajdu, I., Ciccia, A., Lewis, S.M. & Elledge, S.J. Wolf-Hirschhorn syndrome candidate 1 is involved in the cellular response to DNA damage. *Proc Natl Acad Sci U S A* **108**, 13130-13134 (2011).
113. Dulev, S., Tkach, J., Lin, S. & Batada, N.N. SET8 methyltransferase activity during the DNA double-strand break response is required for recruitment of 53BP1. *EMBO Rep* **15**, 1163-1174 (2014).
114. Hwang, D.W. *et al*. Chromatin-mediated translational control is essential for neural cell fate specification. *Life Sci Alliance* **1**, e201700016 (2018).
115. Bennardo, N., Cheng, A., Huang, N. & Stark, J.M. Alternative-NHEJ is a mechanistically distinct pathway of mammalian chromosome break repair. *PLoS Genet* **4**, e1000110 (2008).

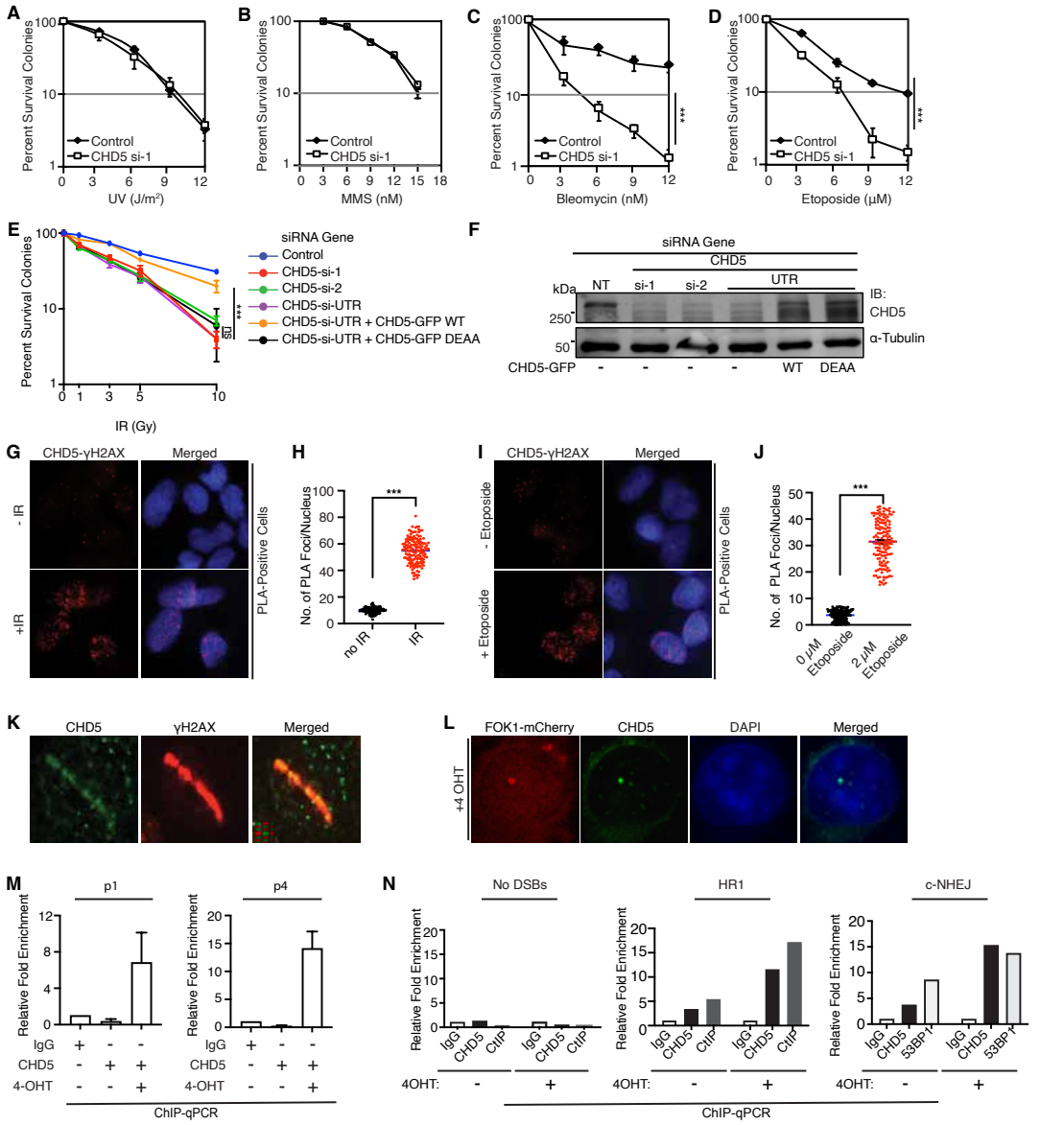


Figure 1. CHD5 ATPase-dependent helicase activity mediates resistance to DNA DSBs and CHD5 localizes and binds to DSBs

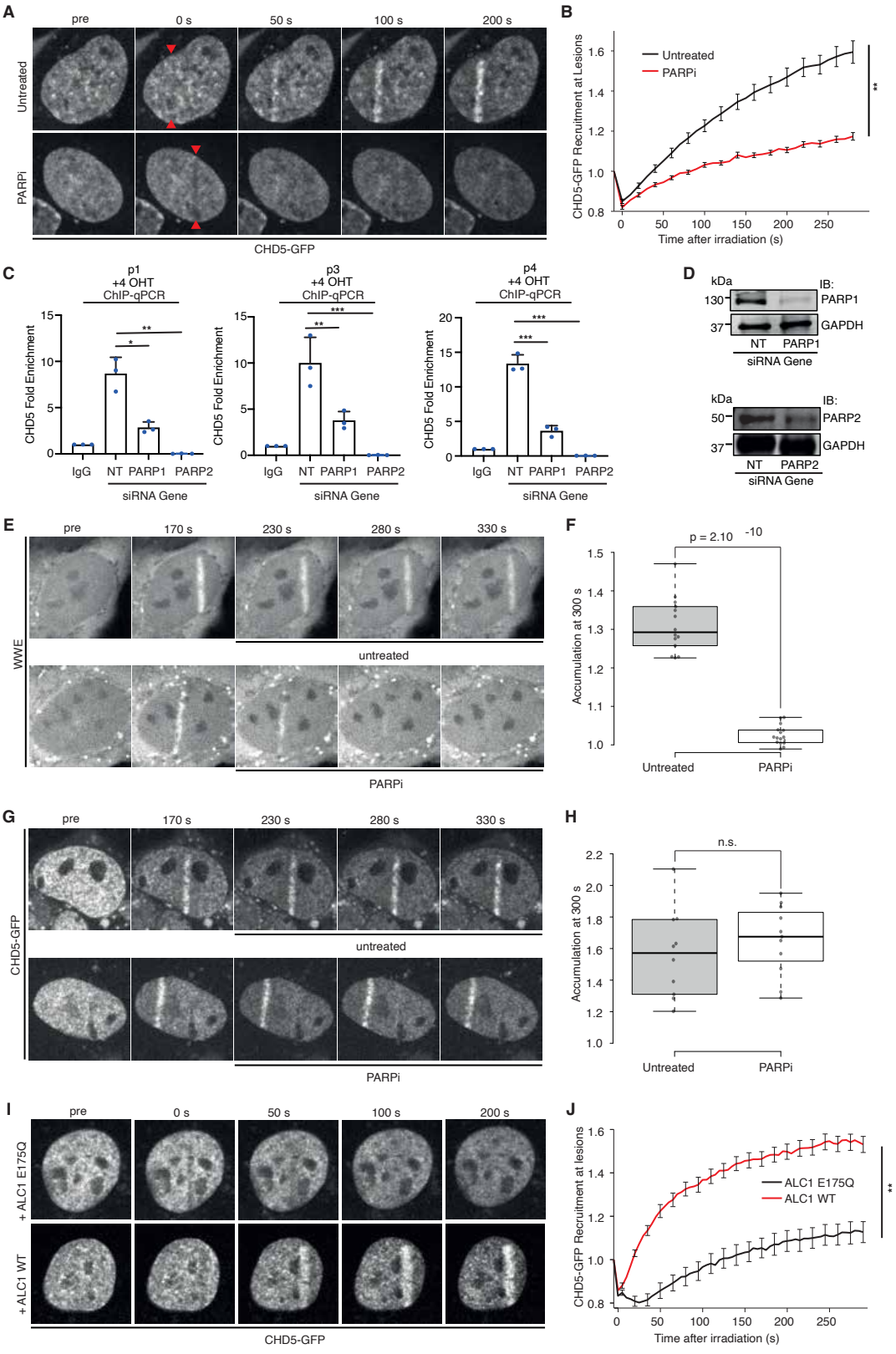


Figure 2. PARP-mediated chromatin relaxation facilitates CHD5 localization to DSBs

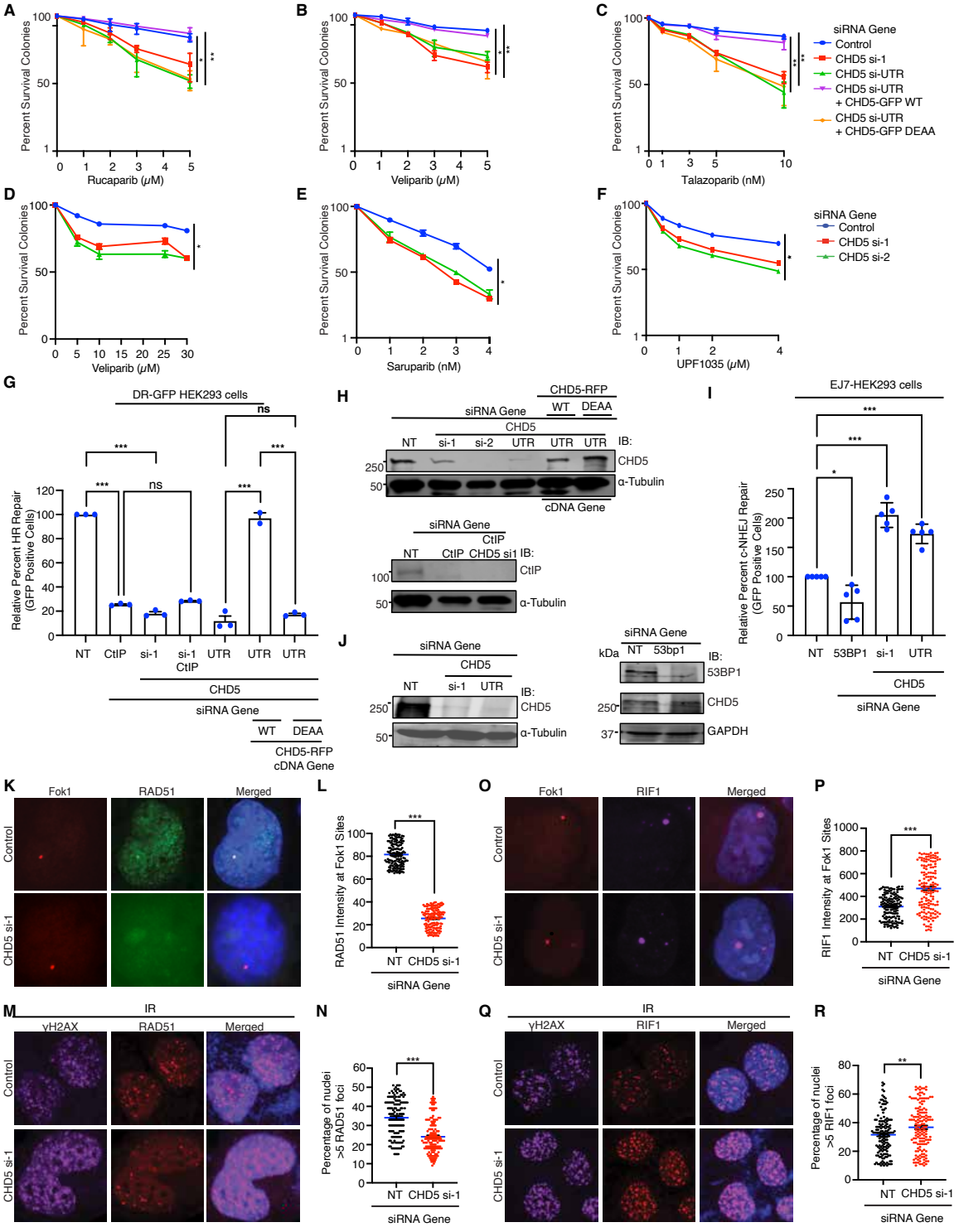


Figure 3. CHD5 directs DSB repair pathway choice

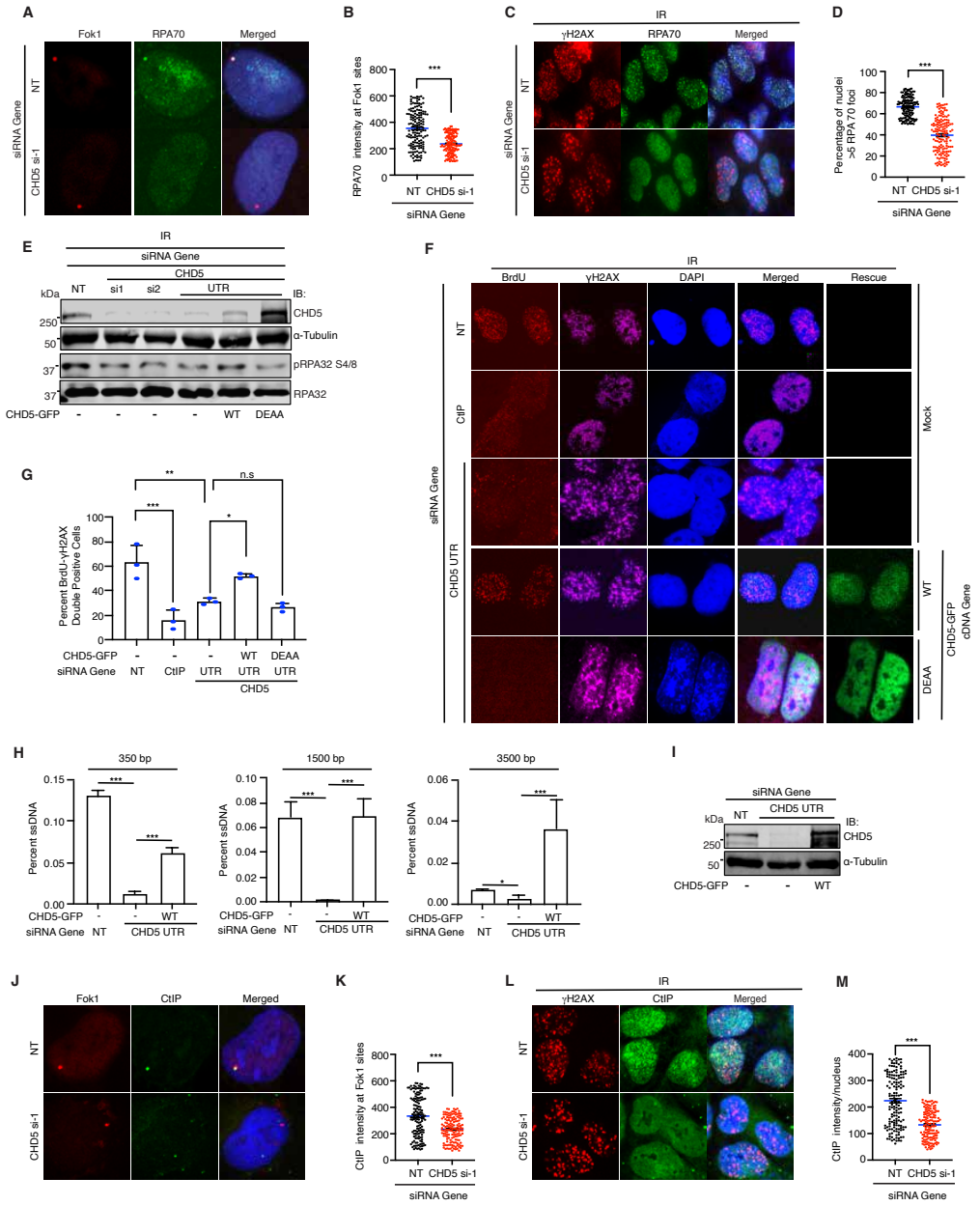


Figure 4. CHD5 helicase activity promotes DNA end resection

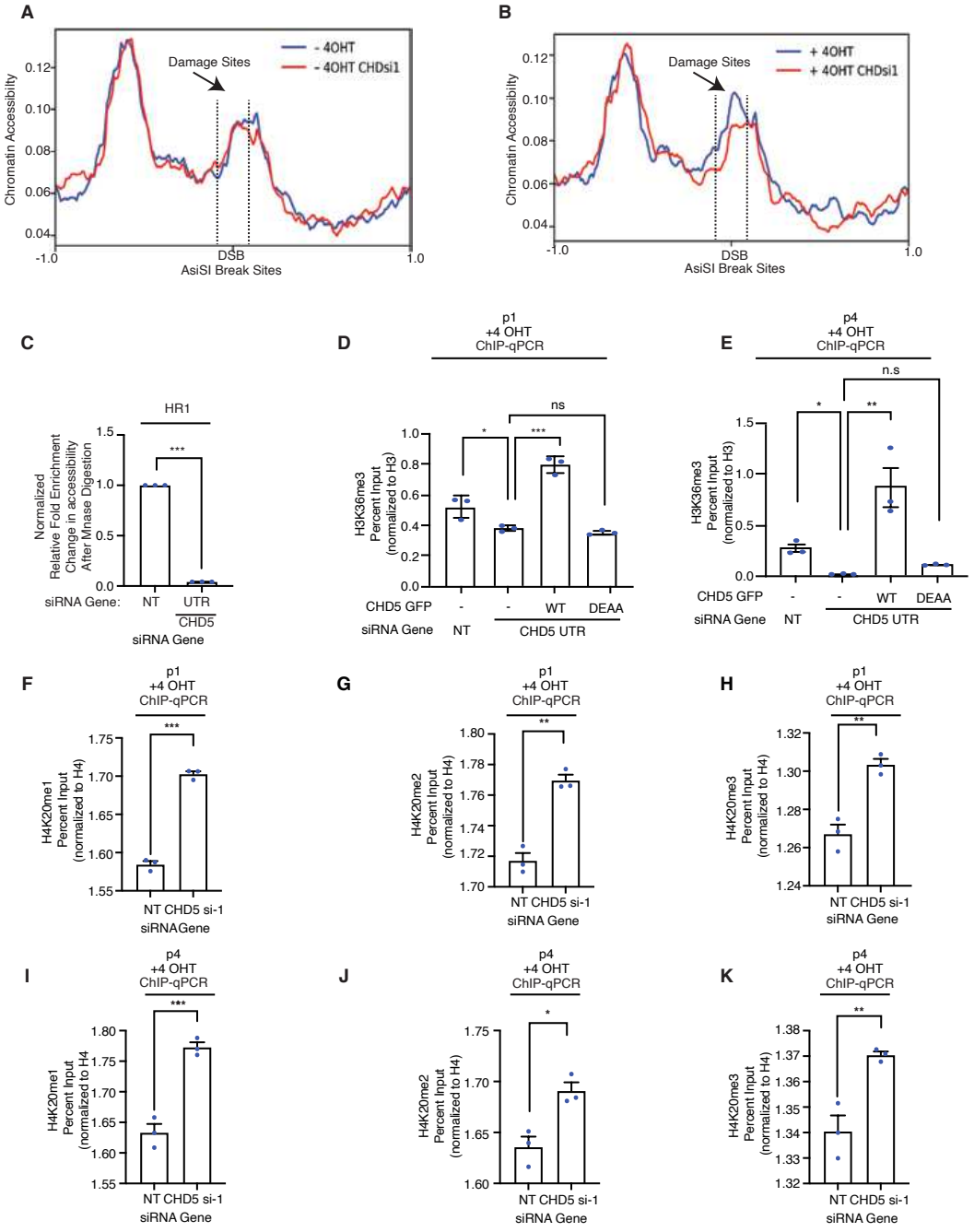


Figure 5. CHD5-mediated chromatin relaxation directs HR and NHEJ histone methylation marks at DSBs

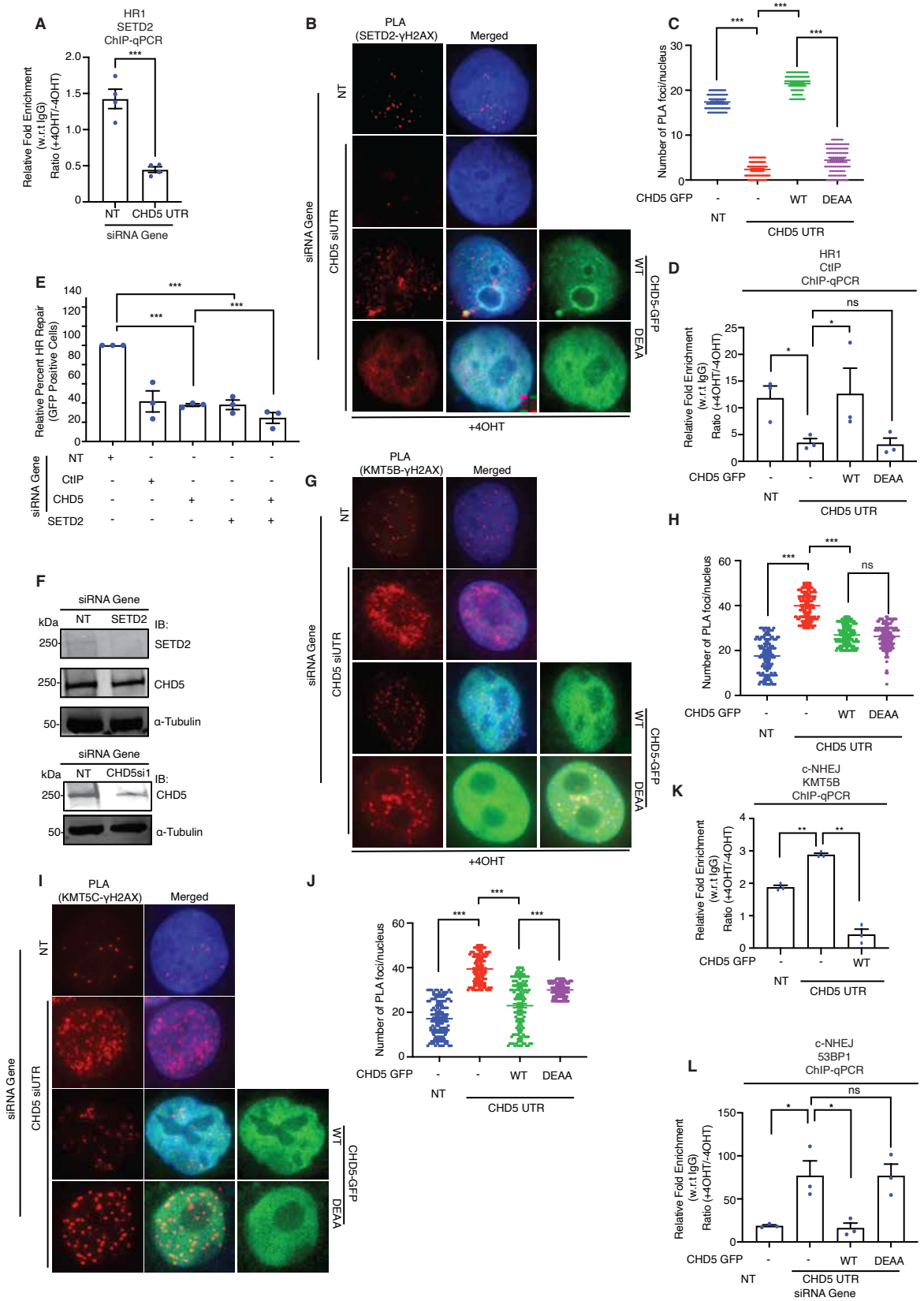


Figure 6. CHD5 directs recruitment of epigenetic writers to facilitate CtIP and 53BP1 binding at DSBs

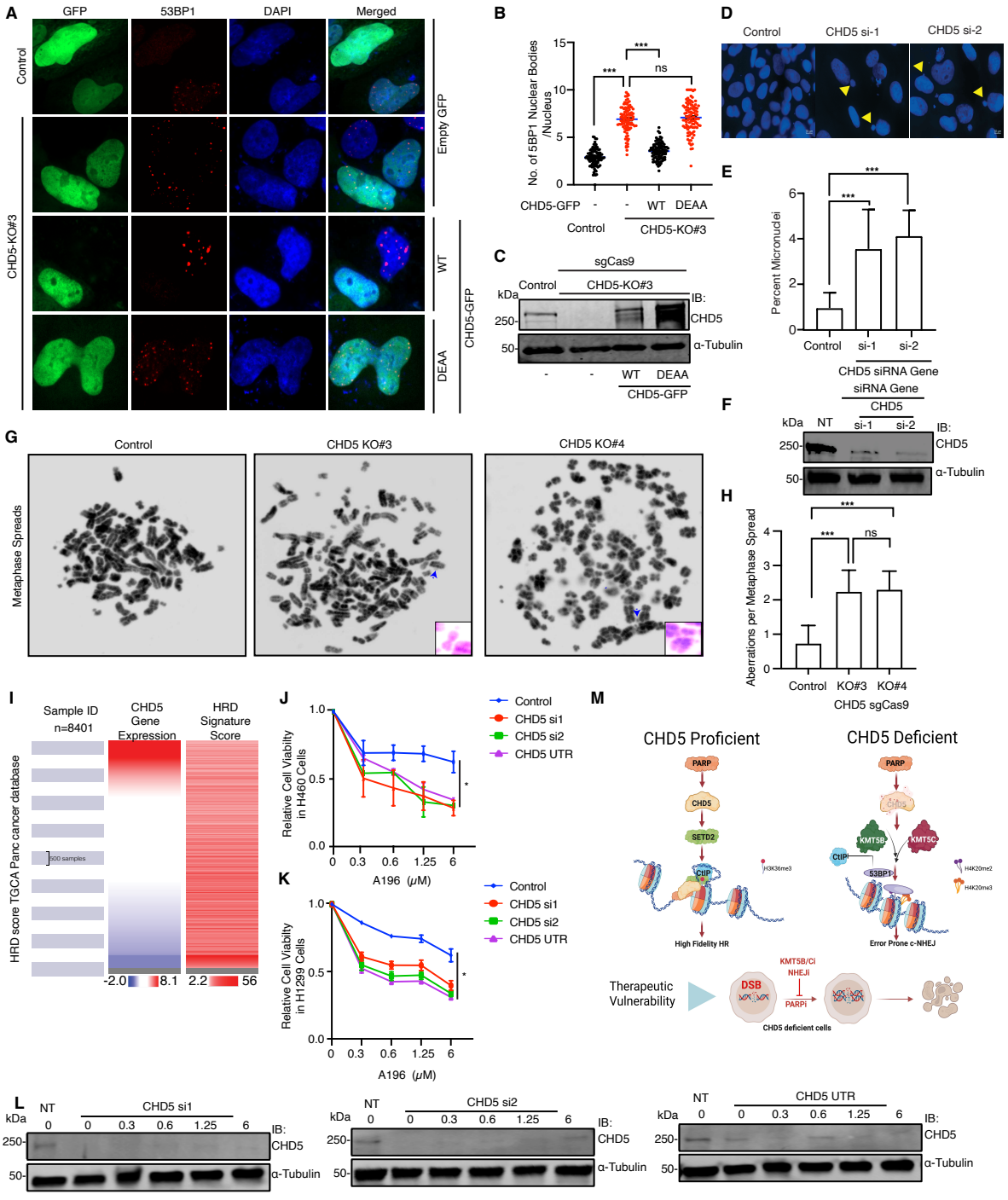


Figure 7. CHD5 dysegulation causes genomic instability and vulnerability to KMT5B/C inhibition

SUPPLEMENTAL DATA

Figure S1. CHD5 ATPase-dependent helicase activity mediates resistance to DSBs and CHD5 localizes and binds to DSBs. A. Colony formation assay in HEK293T cells transfected with two independent CHD5 siRNAs and treated with indicated doses of IR. Data represent mean ± SEM from three independent replicates. ***p < 0.001. **B.** Western blot analysis confirming CHD5 knockdown in HEK293T cells used in panel (A). **C-F**. Colony survival assays in PANC1 (C-D) and H460 cells (E-F) transfected with two independent CHD5 siRNAs and rescued with CHD5-GFP WT or DEAA, following treatment with indicated doses of IR. Data represent mean ± SEM from three independent replicates. *p < 0.01, ***p < 0.001. **G.** Colony formation assay in U2OS *CHD5* WT and KO cells reconstituted with CHD5-GFP WT or DEAA, treated with indicated IR doses. Mean ± SEM from three independent replicates is shown. **p < 0.01. **H.** Western blot confirming CHD5 knockout in U2OS cells used in panel (G). **I-L**. Representative images and quantification of proximity ligation assay (PLA) showing CHD5 and γH2AX co-localization (red foci) in U2OS cells treated with (I–J) UV (6 J/m²) or (K–L) MMS (2 mM). Nuclei were counterstained with DAPI (blue). Quantification was based on 150 nuclei from three independent experiments. **M.** Representative images showing CHD5-GFP or CHD5-FLAG localization to FokI-induced DSBs in U2OS-2-6-5 cells treated with 1 μM Shield-1 and 1μM 4-OHT for 4 h. **N.** Representative IF image showing co-localization of CHD5 (green) and γH2AX (red) at I-SceI–induced DSBs in U2OS-TRE-I-SceI-19 cells. These cells harbor a ~200-copy transgene array (pTRE/I-SceI) adjacent to 96 TRE repeats. Upon tamoxifen induction, Cherry-tTA-ER translocates into the nucleus to activate DSB formation. **O-P**. Representative IF images and quantification showing CHD5 (green), γH2AX (red), and Cyclin A localization at laser-

induced DNA damage sites in U2OS cells. Quantification includes 20–30 cells from three independent experiments. Data are presented as mean ± SEM.

Figure S2. PARP1/2 inhibition and knockdown impair CHD5 localization to DNA damage sites. A-B. Representative images and quantification of CHD5-GFP recruitment to laser-induced DNA damage sites in U2OS cells pretreated for 4 h with either 10 μM olaparib (PARP inhibitor), 10 μM KU-55933 (ATM inhibitor), 10 μM VE-821 (ATR inhibitor), or 10 μM NU7441 (DNA-PKcs inhibitor). **C-D.** Representative images and quantification of CHD5-GFP recruitment to laser-induced DNA damage sites in U2OS cells transfected with the indicated siRNAs targeting PARP1 and PARP2. **E.** HEK293T cells overexpressing CHD5-FLAG or empty vector were IP'ed using anti-FLAG antibody. Input and IP'ed protein were run on SDS-PAGE and immunoblotted with indicated antibodies (PAR and Flag). For **B** and **D**, mean +/- SEM from three independent replicas are shown. ** $p < 0.01$, *** $p < 0.001$.

Figure S3. CHD5 directs DSB repair pathway choice. A-C. Homologous recombination (HR), classical non-homologous end joining (c-NHEJ), and alternative NHEJ (alt-NHEJ) repair efficiencies in U2OS cells harboring DR-GFP (HR), EJ5-GFP (c-NHEJ), and EJ2-GFP (alt-NHEJ) reporter constructs. Cells were transfected with the indicated siRNAs and I-SceI endonuclease and rescued with CHD5-RFP WT or DEAA. Live cells were analyzed by flow cytometry. The RFP-positive population was sorted, and the percentage of GFP-positive cells within this population was used to quantify repair efficiency. Data represent mean ± SEM from three independent replicates. *$p < 0.05$, ***$p < 0.001$. **D.** Cell cycle analysis of U2OS cells transfected with the indicated CHD5 siRNAs. **E.** Western blot confirming CHD5 knockdown and rescue with CHD5-

RFP WT or DEAA in U2OS DR-GFP HR reporter cells used in panel (A). **F.** Western blot confirming CHD5 and 53BP1 knockdown in U2OS EJ5-GFP c-NHEJ reporter cells used in panel (B). **G.** Western blot confirming CHD5 and CHD7 knockdown in U2OS EJ2-GFP alt-NHEJ reporter cells used in panel (C). **H–I.** Representative IF images and quantification of RAD51 (green) and γH2AX (red) foci in U2OS *CHD5* WT and KO cells treated with 10 μM etoposide for 4 h. Each circle represents a single data point; 150 cells were analyzed. ***p < 0.001. **J–K.** Representative IF images and quantification of RIF1 (green) and γH2AX (red) foci in U2OS *CHD5* WT and KO cells treated with 10 μM etoposide for 4 h. Each circle represents a single data point; 150 cells were analyzed. ***p < 0.001. **L-M.** Representative IF images and quantification of RAD51 (green) and γH2AX (red) foci in U2OS *CHD5* WT and KO cells exposed to 10 Gy IR for 4 h. Each circle represents a single data point; 150 cells were analyzed. ***p < 0.001. **N-O.** Representative IF images and quantification of RIF1 (red) and γH2AX (purple) foci in U2OS *CHD5* WT and KO cells exposed to 10 Gy IR for 4 h. Each circle represents a single data point; 150 cells were analyzed. Data in panels (A–C, H–O) represent mean ± SEM from three independent replicates. ***p < 0.001.

Figure S4. CHD5 promotes CtIP and ATRIP localization to DNA damage sites. A-B. Representative IF images and quantification of proximity ligation assays (PLA) detecting co-localization of γH2AX and CHD5 (red foci) in U2OS cells treated with 10 Gy IR for 4 h. Nuclei were stained with DAPI (blue). Each circle represents a single cell; data from a total of 150 cells are shown. **p < 0.01. **C-D.** Representative IF images and quantification of CtIP (purple) and γH2AX (red) foci in U2OS CHD5 WT and KO cells treated with 10 Gy IR for 4 h. Each circle represents a single cell; data from a total of 150 cells are shown. **p < 0.01. **E-F.** Representative

images and quantification of GFP-CtIP recruitment to laser-induced DNA damage sites in U2OS cells transfected with the indicated CHD5 siRNAs. *p < 0.05. **G-H.** Representative images and quantification of GFP-ATRIP recruitment to laser-induced DNA damage sites in U2OS cells transfected with the indicated CHD5 siRNAs. Data in panels (A–H) represent mean ± SEM from three independent replicates. *p < 0.05, **p < 0.01.

Figure S5. CHD5-mediated chromatin relaxation directs HR and NHEJ histone methylation marks at DSBs. A-C. ChIP-qPCR analysis showing enrichment of H3K36me1 (A), H3K36me2 (B), and H3K36me3 (C) at HR-prone repair sites in DIvA cells transfected with CHD5 or NT siRNA, rescued with CHD5-GFP WT or DEAA, and treated with or without 4-OHT for 4 h. **D-F.** ChIP-qPCR analysis showing enrichment of H4K20me1 (D), H4K20me2 (E), and H4K20me3 (F) at NHEJ-prone repair sites in DIvA cells transfected with CHD5 or NT siRNA and treated with 4-OHT for 4 h. **G.** Representative western blot analysis of H3K36me1, H3K36me2, H3K36me3, H4K20me1, H4K20me2, and H4K20me3, as well as total histone H3 and H4 expression, in U2OS DIvA cells transfected with indicated CHD5 siRNAs and rescued with CHD5-RFP WT or DEAA, treated with or without 4-OHT, corresponding to panels (A–F). Data in panels (A–F) represent mean ± SEM from three independent replicates. *p < 0.05, **p < 0.01.

Figure S6. CHD5-mediated chromatin relaxation directs recruitment of epigenetic writers to facilitate CtIP and 53BP1 binding at DSBs. A-D. qPCR analysis of NSD1, NSD2, NSD3, and SETD2 mRNA expression levels following CHD5 knockdown in U2OS cells. **E-F.** ChIP-qPCR analysis showing CtIP enrichment at p1 and p4 DSB sites in U2OS-265 cells transfected with CHD5 or NT siRNA and rescued with CHD5-GFP WT or DEAA, following treatment with

4-OHT for 4 h. **G-H**. Representative PLA images and quantification showing KMT5A–γH2AX co-localization in U2OS DIvA cells treated with 500 nM 4-OHT for 4 h. Nuclei were stained with DAPI (blue). Quantification was based on 50 nuclei from three independent replicates. **I-K.** qPCR analysis of KMT5A, KMT5B, and KMT5C mRNA expression levels following CHD5 knockdown in U2OS cells. **L-O.** ChIP-qPCR analysis showing 53BP1 and RIF1 enrichment at p1 and p4 DSB sites in U2OS-265 cells transfected with CHD5 or NT siRNA and treated with 4-OHT for 4 h. For panels (A–F) and (I–O), data represent mean ± SEM from three independent replicates. *$p < 0.05$, **$p < 0.01$, ***$p < 0.001$.

Figure S7. CHD5 dysregulation promotes genomic instability and sensitizes NSCLC cells to NHEJ inhibitors. A, C. Representative IF images and quantification of 53BP1 nuclear bodies (green) in Cyclin A-negative (red) U2OS cells treated with the indicated CHD5 siRNAs. Data represent mean ± SEM from three independent replicates. ***$p < 0.001$. **B, D.** Representative IF images and quantification of 53BP1 nuclear bodies (green) and spontaneous γH2AX foci (red) in H460 cells treated with the indicated CHD5 siRNAs. Data represent mean ± SEM from three independent replicates. ***$p < 0.001$. **E-G.** Correlation of CHD5 mRNA expression with mutation count (E), tumor mutational burden (TMB) (F), and aneuploidy score (G) in a cohort of 10,953 cancer patients from the c-Bio-Portal database. **H-K.** Representative IF images and quantification of 53BP1 or RIF1 (green) and γH2AX (red) foci in H460 cells transfected with the indicated CHD5 siRNAs and exposed to 4 Gy IR for 4 h. A total of ~450 cells were analyzed from three independent experiments. Data represent mean ± SEM. ***$p < 0.001$. **L–N.** Cell viability assay in H460 cells transfected with CHD5 or NT siRNAs and treated with increasing concentrations of (H) NU7441 (DNA-PKcs inhibitor), (I) SCR-7 (DNA Ligase IV inhibitor), or (J) L189 (DNA Ligase I/III/V

inhibitor), followed by exposure to 4 Gy IR. Cell viability was assessed 72 h post-treatment using the Alamar Blue assay. **O.** Western blot confirming CHD5 knockdown in H460 cells used in panels H–N.

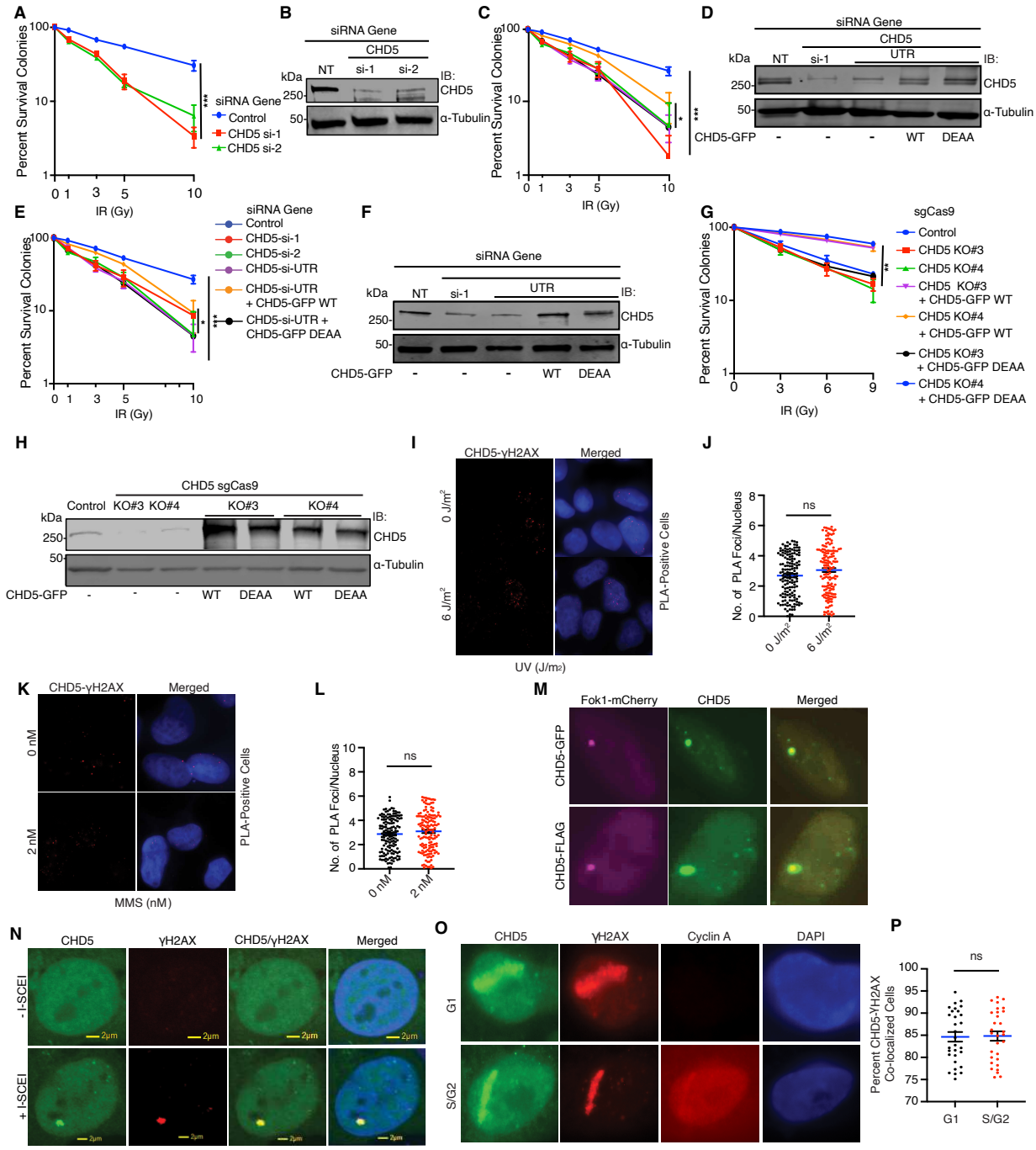


Figure S1. CHD5 ATPase dependent helicase activity mediates resistance to DSBs and CHD5 localizes and binds to DSBs

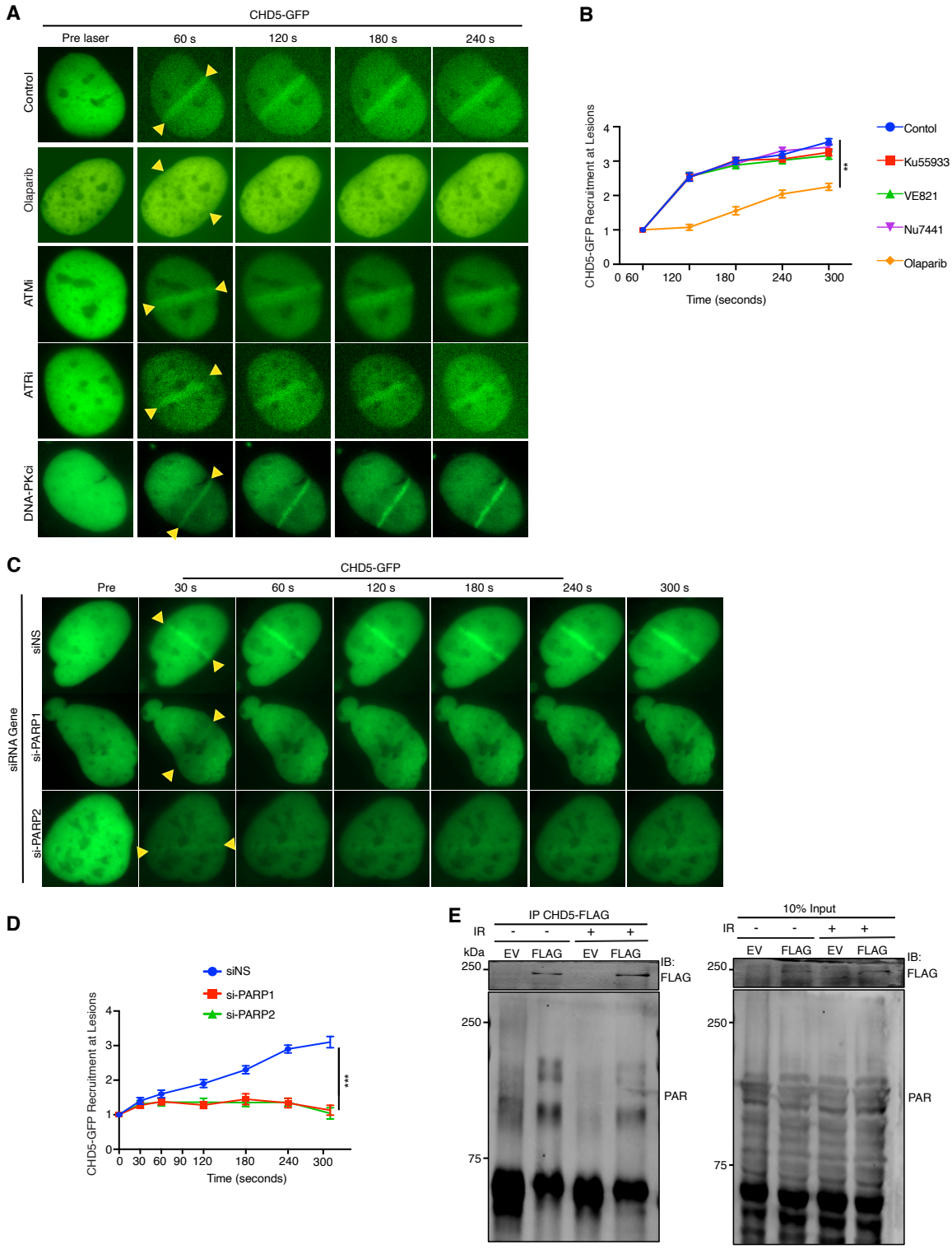


Figure S2. PARP1/2 inhibition and knockdown impairs CHD5 localization to DNA damage sites

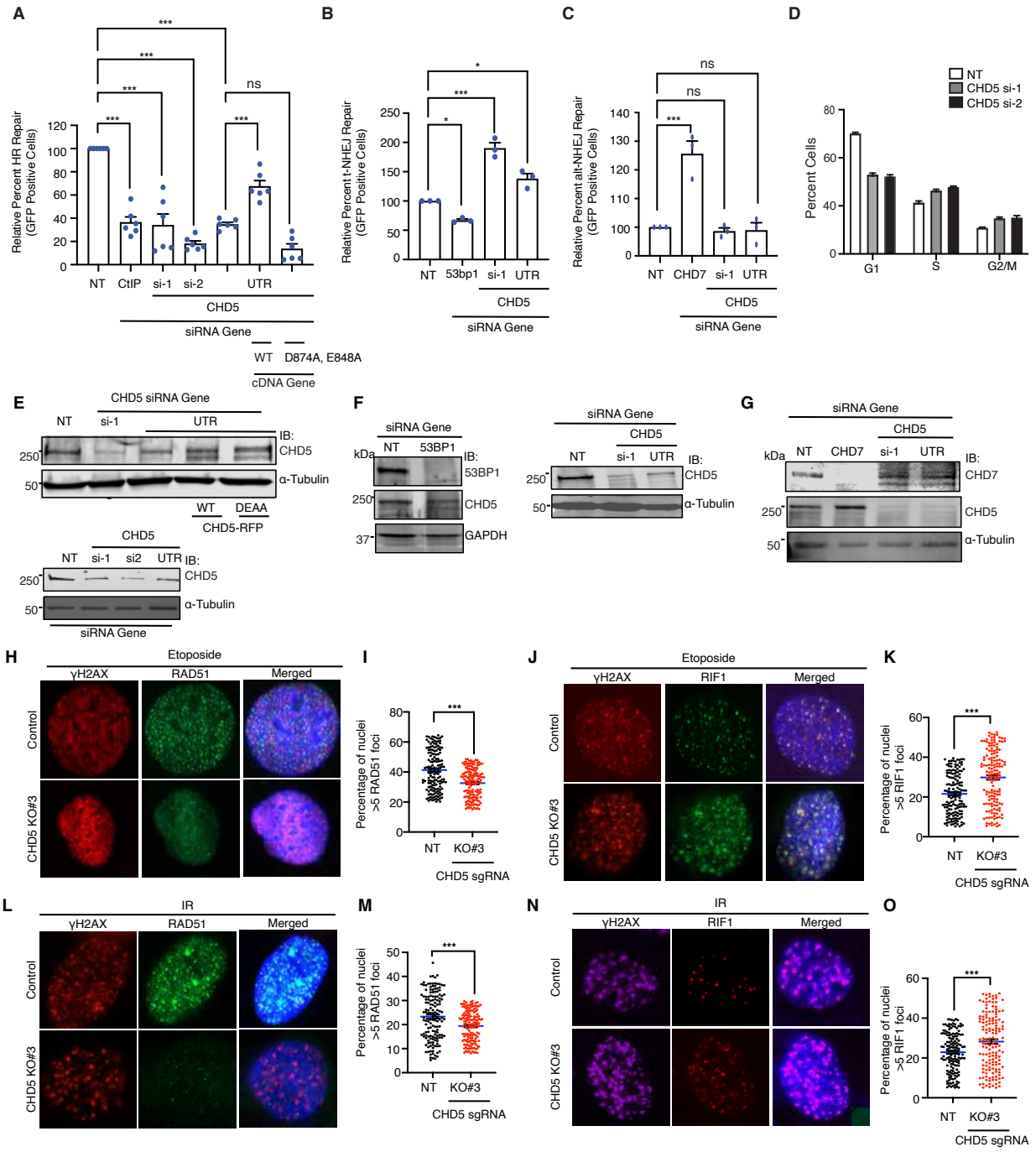


Figure S3. CHD5 directs DNA repair pathway choice

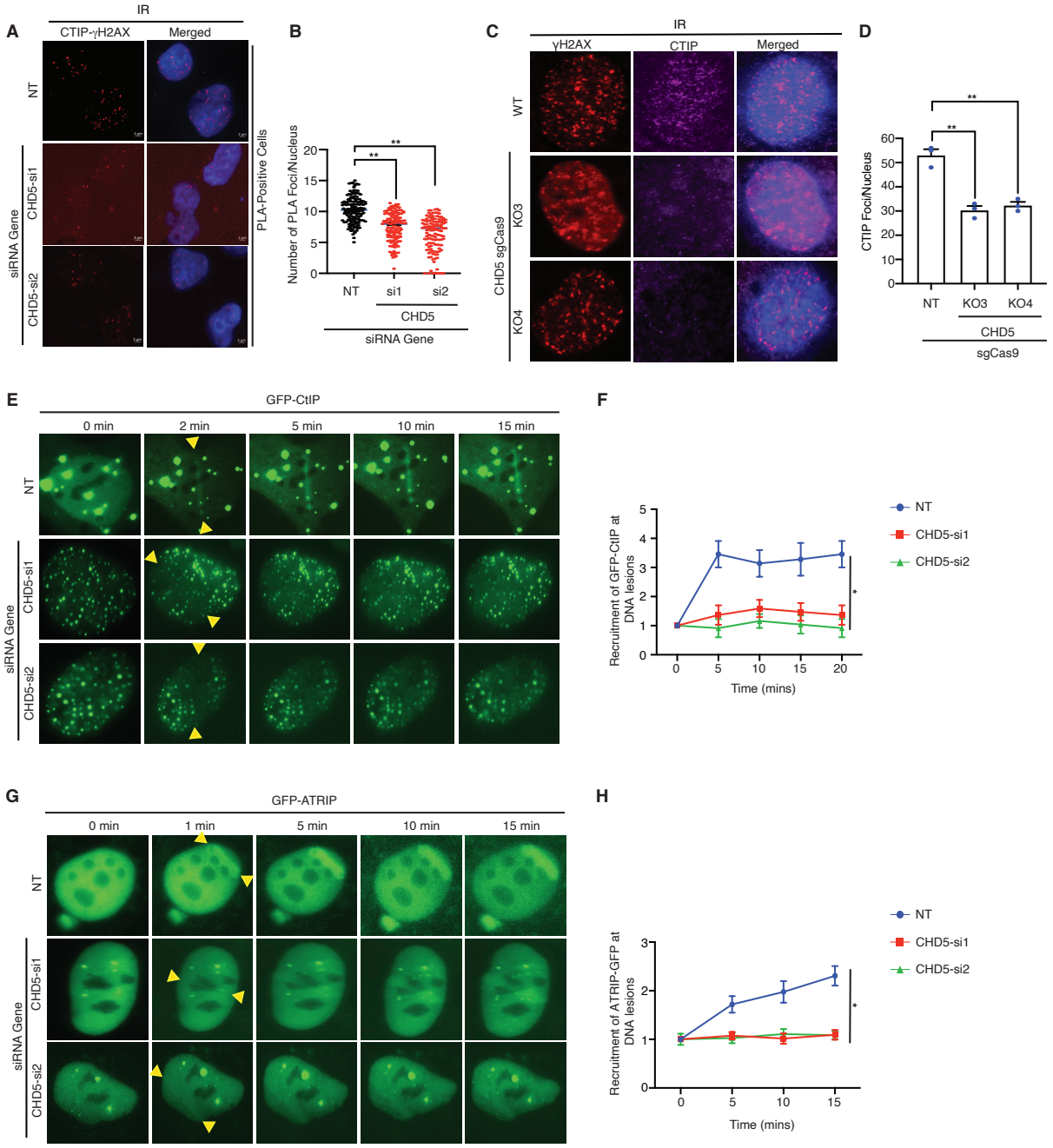


Figure S4. CHD5 promotes CtIP localization to DNA damage sites

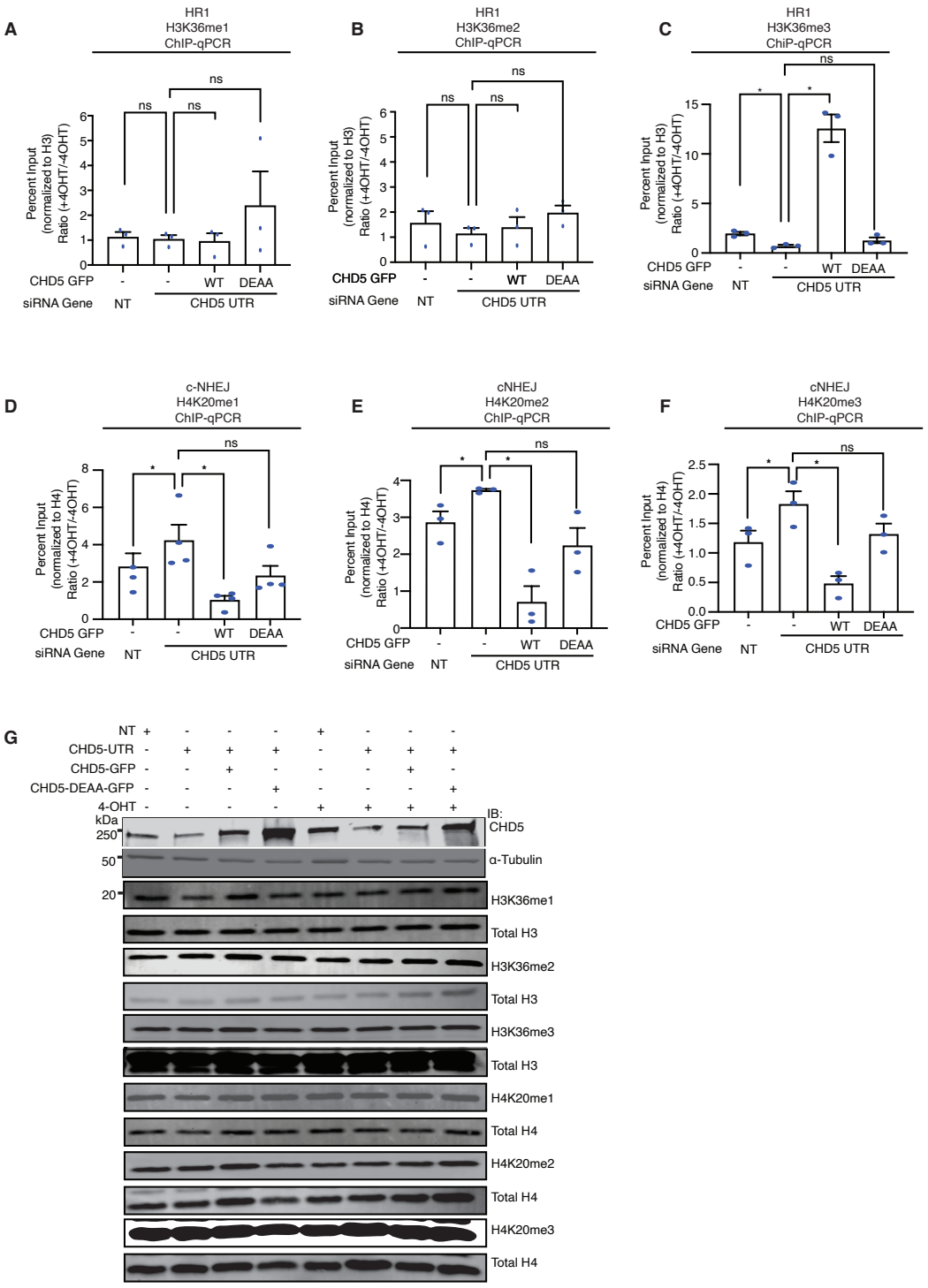


Figure S5. CHD5-mediated chromatin relaxation directs HR and NHEJ epigenetic marks at DSBs

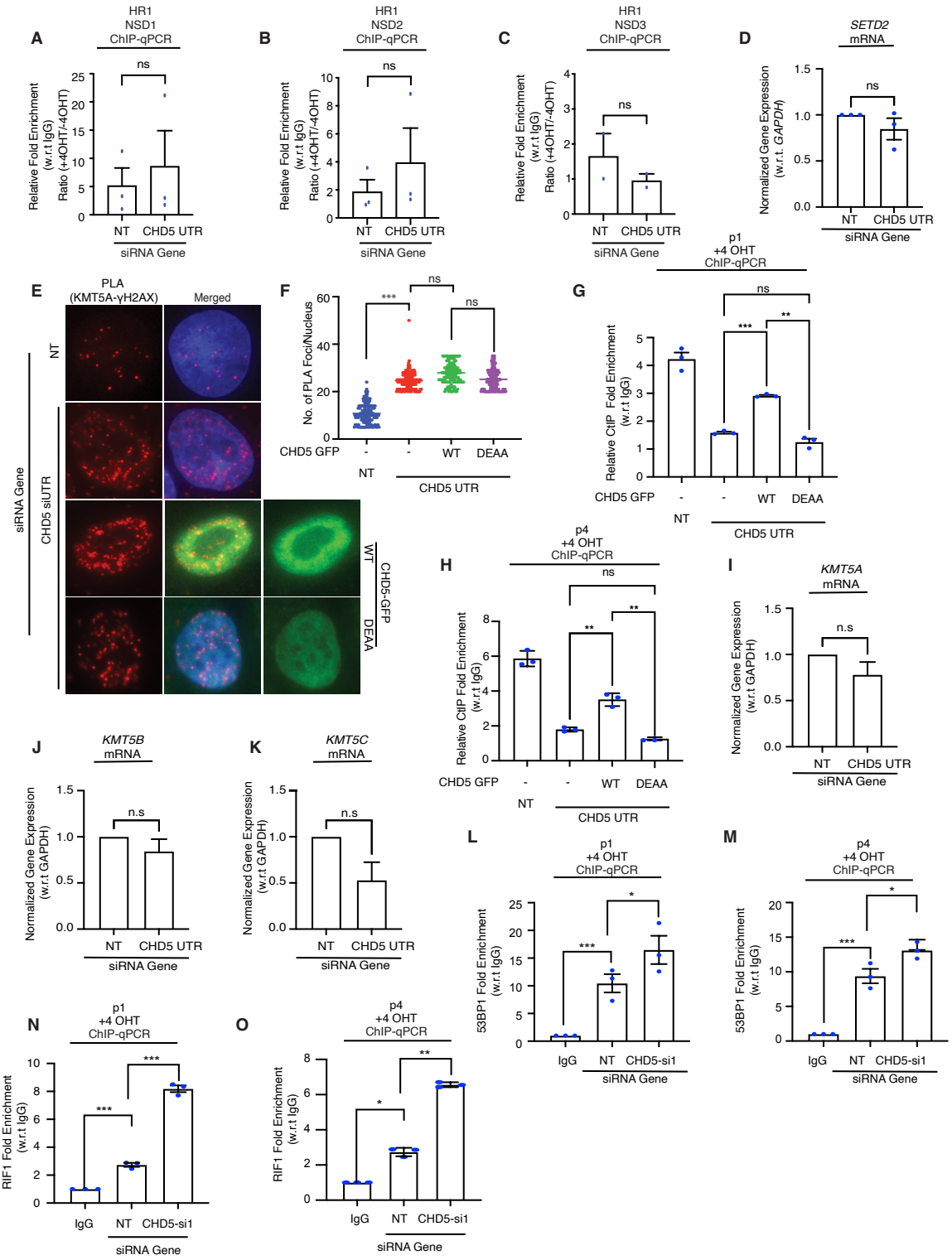


Figure S6. CHD5 directs recruitment of epigenetic writers to facilitate CtIP and 53BP1 binding at DSBs

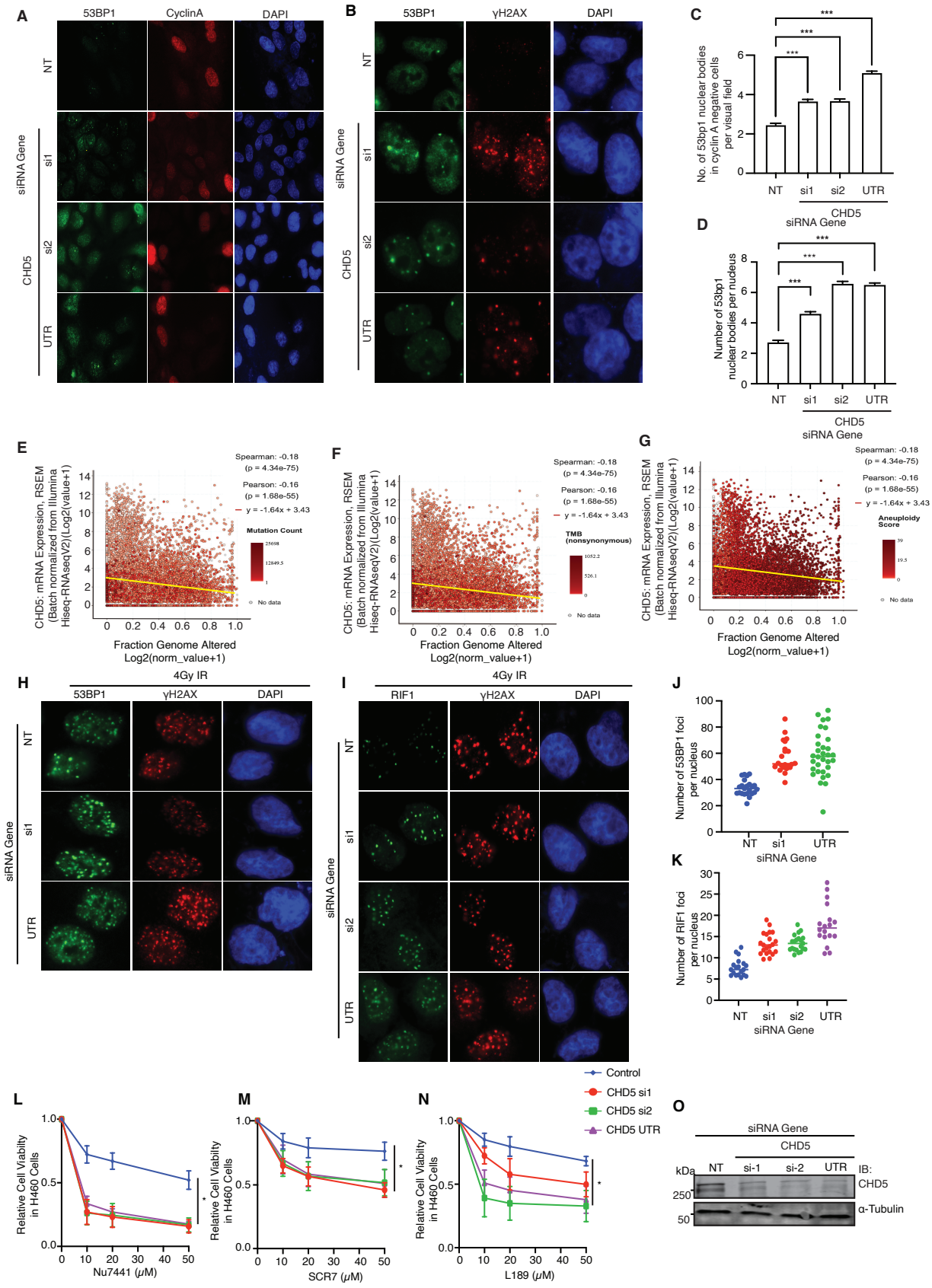


Figure S7. CHD5 dysregulation causes genomic instability and susceptibility to NHEJ inhibition

Supplementary Files

This is a list of supplementary files associated with this preprint. Click to download.

- Table4RTqPCRprimers.xlsx
- Table5Antibodies.xlsx
- Table3ssDNAprimers.xlsx
- TablesforprimersandsiRNAsequence.xlsx
- Table6Enzymes.xlsx
- Table2ChIPPrimers.xlsx
- ReportingSummary.pdf